2016

Numerical Simulation of Conjugate Natural Convection and Radiation within Thermal Wellbore Annuli

Lu, Xueying

UNIVERSITY OF CALGARY

Numerical Simulation of Conjugate Natural Convection and Radiation within Thermal Wellbore Annuli

by

Xueying Lu

A THESIS

SUBMITTED TO THE FACULTY OF GRADUATE STUDIES

IN PARTIAL FULFILLMENT OF THE REQUIREMENTS FOR THE

DEGREE OF MASTER OF SCIENCE

GRADUATE PROGRAM IN CHEMICAL AND PETROLEUM ENGINEERING

CALGARY, ALBERTA

August, 2016

Abstract

In the petroleum industry, accurately simulating wellbore heat loss through hot fluid injection remains a critical problem as heat transfer and fluid dynamics within the annulus space is complicated. In this study a 2D transient mathematical model is proposed for the conjugate natural convection and radiation within wellbore annuli. The governing equations consist of a vorticity transfer equation, a stream function equation, an energy balance equation and a radiative transfer equation. A finite volume approach with second order upwind scheme is implemented for discretization. Newton-Raphson iteration is deployed for linearization. The algorithm is validated by consistency in simulation results compared with literature. Parameters such as the aspect ratio, radius ratio, radiation and dimensionless time are examined. A case study on vacuum insulated tubing heat transfer using Marlin Well A-6 data showed the merits of the developed program by the consistency of simulation results compared with field measurements.

Acknowledgements

First and foremost I would like to express my deepest gratitude to my supervisor, Professor Zhangxing (John) Chen. His excellent supervision and insightful suggestions have cultivated my interests in studying these fascinating research topics, and guided me through my graduate studies. Moreover, Dr. Chen's utmost encouragement and continuous support have provided me the confidence to pursue research in the broad subject of reservoir simulation. Dr. Chen has a rigorous attitude towards academics and a kind manner to all his students. What I have gained from him is not only knowledge, but also how to be a precise, open-minded, passionate, persistent and supportive scholar.

I would also like to thank all the professors in the department who offered me generous help in both my coursework and research. In particular I am very grateful to Professor S.M. Farouq Ali, for his suggestions on my research and his invaluable support in my academic career.

I would also like to thank Mr. Wanqiang Xiong, a PhD student in our research group, who introduced me to wellbore simulation. His suggestions and guidance on coding, and his collaborations on the coupling of the program developed in this study to a standalone thermal wellbore simulator are appreciated.

Dr. Hui Liu, Dr. He Zhong, Dr. Jia Luo and Dr. Kun Wang must be acknowledged for their insightful discussions and constructive suggestions. I learned so much about reservoir simulation techniques from them.

I also want to thank all my colleagues in the Reservoir Simulation Group for their help throughout my Master's study program. Thanks all my friends in Calgary for their companionship. I will always remember the laughter we shared.

Most importantly, I would like to thank my parents and grandparents for their

unconditional love, support and trust. They are also my life-long mentors, from whom I learned worthy goals in life, and good merits to be preserved. I also thank my boyfriend, Linquan Zhang, for his company, support and love throughout the journey.

Table of Contents

List of Tables

List of Figures

List of Symbols, Abbreviations and Nomenclature

Symbol	Definition
c_p	specific heat capacity, J/(kgcot K)
g	gravitational constant, ($= 6.67408 \times 10^{-11}\mathrm{m}^3\mathrm{kg}^{-1}\mathrm{s}^{-2}$)
Gr	Grashof number ($= g\beta\Delta T L^3/\nu^2$)
H	aspect ratio ($= l/L$)
I	dimensionless intensity
i_0	zero moment of intensity, W/sr
k	thermal conductivity, W/(mK)
l	cylinder height, m
L	annulus radius gap width ($= r_o - r_i$), m
Mmax	number of grids in the mesh along axial direction
N	conduction-to-radiation parameter ($= k\sigma_a/4\sigma T_i^3$)
Nmax	number of grids in the mesh along radial direction
Nu	Nusselt number
Nu_i	local Nusselt number at inner cylinder wall
Nu_o	local Nusselt number at outer cylinder wall
$\overline{\mathrm{Nu}}$	average Nusselt number
p	dimensionless pressure
p'	original pressure, Pa
Pr	Prandtl number ($= \nu/\alpha$)
r	dimensionless radius
r'	original radius, m

r_i	inner cylinder radius, m
r_o	outer cylinder radius, m
R	$= r\kappa_l + 1$
Ra	Rayleigh number ($= g\beta\Delta T L^3/\nu\alpha$)
t	dimensionless time
t'	original time, s
T	dimensionless temperature
T'	original temperature, K
T_i	inner cylinder wall temperature, K
T_o	outer cylinder wall temperature, K
T_f	$= T_i/(T_i - T_o)$
u	dimensionless radial velocity
u'	original radial velocity, m/s
U_{to}	overall heat transfer coefficient, W/m^2 °C
w	dimensionless axial velocity
w'	original axial velocity, m/s
z	dimensionless height
z'	original height, m
Δr	dimensionless radial grid length
Δt	dimensionless time step
Δz	dimensionless axial grid length

Greek Symbols

α	thermal diffusivity, ($= k/(\rho c_p)$) m^2/s
β	thermal expansion coefficient, 1/K
ζ	dimensionless vorticity
κ	radius ratio ($= r_i/r_o$)

κ_l	$= (1 - \kappa)/\kappa (= L/r_o)$
μ	dynamic viscosity, kg/(m·s)
ν	kinetic viscosity, m^2/s
π	Pi ($\approx 3.14159265358979323846$)
ρ	density, kg/m^3
σ	StefanBoltzmann constant, 5.670367×10^{-8} Wm^2K^4
σ_a	absorption coefficient, 1/m
τ_0	optical thickness ($= \sigma_a L$)
ψ	dimensionless stream function

Nomenclature

APB	annulus pressure buildup
CFD	computational fluid dynamics
RTE	radiative transfer equation
SUS	second-order upwind scheme
VIT	vacuum insulated tubing

Chapter 1

INTRODUCTION

1.1 Overview

In the petroleum industry, a wellbore plays a critical role in recovery practice, it is the only means of communication between surface facilities and the underground reservoir. In conventional reservoir simulation, the basic purpose of wellbore modelling is to provide sink/ source terms for the reservoir model. Modern wells are evolved from a simple vertical well. Modern, sophisticated wells include horizontal wells, multilateral wells, wells with vacuum insulated tubing (VIT), and wells with multiple tubing or strings. Sophisticated wells are considerably more expensive to drill and complete; and their use must be justified by a corresponding increase in economic recovery [29]. For this reason, a rigorous wellbore model that can simulate the dynamic and thermal behaviour at all locations, with a reasonable degree of accuracy, is required.

Thermal recovery processes involving steam injection are popular with the heavy oil industry. Crude oil viscosity decreases sharply as temperature increases. Steam is injected into the subsurface to carry heat to the reservoir, reduce oil viscosity, provide drive energy and thereby improve the displacement efficiency of injected fluid [19]. In the steam injection process, the steam condition at the sandface is one of the critical parameters for reservoir simulation and management. To obtain information about the steam condition, fluid flow and heat transfer of wellbore must be accurately modelled.

Modelling wellbore dynamics and thermal behaviour has many critical applications. In well completion design, the estimation of tubing, casing, cementing tem-

perature and the thermal stress induced is required to determine the tubing/ casing size, material, type of insulation under specific operating conditions. A proper cement placement job requires knowledge of the bottom hole circulating temperature (BHCT), the hot spot depth (the depth where temperature is highest), and the overall temperature profile [3]. Estimation of annulus pressure build-up (APB), which is caused by the thermal expansion of annulus fluid, is another important application of these models, because APB related failures have occurred with improperly designed wells [9].

Modelling wellbore fluid flow and heat transfer with a decent degree of accuracy is not an easy task. Within the wellbore the complicates, strongly coupled, nonlinear nature of the fluid dynamics and heat transfer mechanisms are challenging. Mathematical modelling of thermal wellbore can be dated back to Ramey (1962) who presented an analytical approximation solution of wellbore fluid temperature and pressure distribution, outer tubing wall temperature and inner casing wall temperature, as functions of production time and well depth [54]. Ramey's model consists of three parts: 1) fluid flow and heat transfer within wellbore tubing, 2) heat transfer from the tubing wall up to the casing/cementing boundary, and 3) heat transfer in the surrounding formation. This formulation became fundamental to subsequent research in thermal wellbore modelling. Research is often carried out by relaxing Ramey's assumptions to model more complex wellbores.

The state-of-the-art thermal wellbore models are able to simulate transient thermal multiphase flow [4][7][3][69]. The governing equations contain coupled mass, momentum and energy balance equations. A drift-flux model is applied to capture the slip phenomenon between phases. The time- and depth- dependent overall heat transfer coefficient that represents a series of thermal resistance from tubing wall to the cementing/formation interface is supplemented as a source term in the wellbore

energy balance equation. Heat transfer in the formation is modelled by a 2D heat conduction equation [20][7].

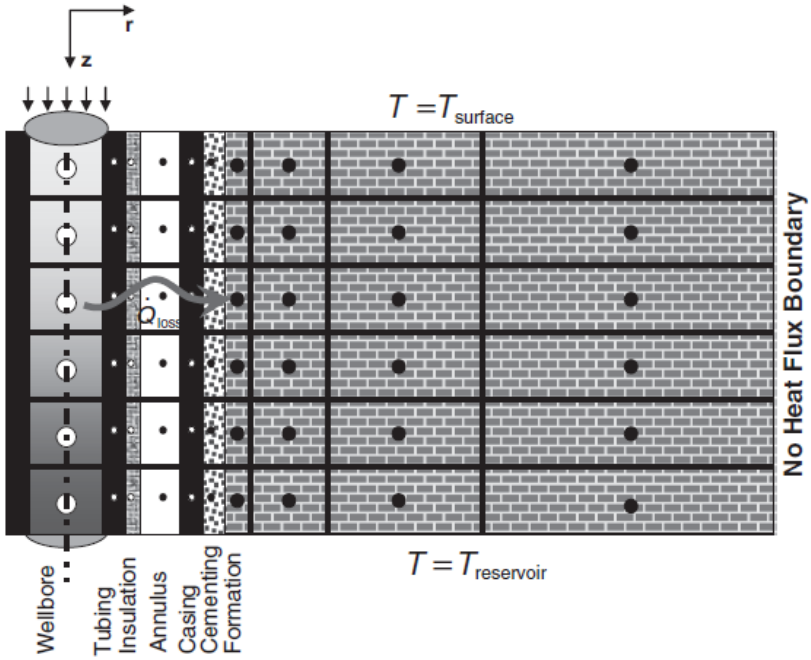

Figure 1.1: Schematic of state-of-the-art discretized thermal wellbore model, subtracted from Bahonar 2010 [4]

The accuracy of the overall heat transfer coefficient significantly affects the model's efficiency in wellbore heat transfer analysis. The heat transfer mechanisms between the flowing fluid and the cement-formation interface includes: conduction within tubing and casing wall, conduction within cement and convection and radiation within the annulus [65]. Among these mechanisms, the convective and radiative heat transfer within the annulus is the most difficult to simulate, because of the complex fluid dynamics and its high dependence on the annulus space geometry and boundary conditions. In fact, natural convection in an enclosure is one of the major problems in Computational Fluid Dynamics (CFD) [57].

To the author's knowledge, in the literature on thermal wellbore modelling, the

heat transfer within wellbore annulus is accounted for using empirical correlations. The method for estimating the overall heat transfer coefficient was proposed by Willhite in 1967 [65]. In this method, the annulus convective heat transfer is calculated using a correlation obtained from experiments on natural convection between two parallel vertical plates. The radiative heat transfer is calculated based on Stefan-Bolzmann law [45]. Willhite's method for calculating an over all heat transfer coefficient historically satisfied the needs of industry. However, as more sophisticated wells with dual tubing or with insulated tubing are in use, there is a growing need to apply CFD techniques to insure accurate and versatile wellbore model.

The primary objective of this study is to use CFD techniques to simulate the conjugate natural convection and radiation within thermal wellbore annuli. The proposed 2D transient model couples the mass conservation equation, the vorticity-stream function formulation of 2D Navier-Stokes equations, the energy balance equation and the radiative transfer equation. A finite volume discretization scheme is implemented with second-order upwind scheme for the convection terms. The discretized system is solved fully implicitly and coupled. The numerical schemes are validated by replicating a series of tests from the literature, preserving high efficiency at high Rayleigh numbers (Ra=1E7). The effects of aspect ratio, radius ratio, radiation and time on the flow structure and heat transfer characteristics are examined. The program is developed in C++. The objective-oriented programming allows the program to be conveniently coupled with other thermal wellbore simulators. A case study is carried out simulating vacuum insulated tubing heat transfer using a stand alone wellbore simulator [69] coupled with the developed annulus heat transfer program. The simulated results match remarkably well with the field experimental data, validating the merits of this study.

1.2 Thesis Outline

Chapter 2 consists of a literature review. Initially the history of thermal wellbore modelling and simulator development are reviewed; the associated milestones are identified. Then the computational fluid dynamics techniques used to solve natural convection problems, and Navier-Stokes Equations are reviewed. In addition, the vacuum insulated tubing (VIT) heat transfer characteristics are reviewed in preparation for the case study.

In Chapter 3, the mathematical model and the numerical schemes to simulate the conjugate natural convection and radiation within a thermal wellbore annulus are elaborated. First governing equations are constructed in primary variables (i.e. pressure, temperature, velocities and intensity), that contain 2D transient Navier-Stokes equations as the momentum balance equations. The the governing equations are then derived in secondary variables, (i.e. stream function, vorticity, temperature and intensity). After that the discretization schemes and numerical algorithm are explained in detail.

The proposed numerical algorithm is validated in Chapter 4 by replicating a group of tests in the literature. Simulation results including average Nussult numbers and velocities are compared with the literature outcomes and consistency is found. This reinforces confidence in the developed algorithm. Then a group of numerical experiments are carried out to examine the effect of aspect ratio, radius ratio, intensity of radiation and dimensionless time on the flow structure and heat transfer characteristics.

Chapter 5 presents a case study on vacuum insulated tubing heat transfer simulation using a stand alone wellbore simulator [69] coupled with the developed program. Marlin Well A6 data [23] are used in the study. The simulation results match well with the field data considered.

All the findings are summarized in Chapter 6 followed by suggestions for further research.

Chapter 2

LITERATURE REVIEW

2.1 Development of Thermal Wellbore Modelling

The first mathematical wellbore model was formulated by Ramey in 1962 [54]. He assumed single phase steady-state incompressible tubing fluid flow, fixed fluid and formation properties, with no frictional loss or kinetic energy effect. Then he presented an analytical solution of wellbore fluid pressure and temperature, outer tubing and casing wall temperature as functions of production time and well depth. Ramey pointed out two critical issues in the formulation of wellbore model to estimate heat loss: 1) the overall heat transfer coefficient from inner tubing wall to the cementing/-formation boundary, 2) time function that characterizes the formation heat transfer behaviour due to its relatively large thermal conductivity compared to wellbore fluids and materials. Since then, Ramey's work has built the foundation of thermal wellbore modelling and his formulation of the model has been adopted in many subsequent studies.

In 1967, Willhite [65] proposed the well-known iterative method for calculating the overall heat transfer coefficient that has widely been used by industry. For a wellbore, the overall heat transfer coefficient expresses the combined effect of the series of thermal resistances between the flowing fluid and the cement-formation interface. The overall heat transfer coefficient accounts for, in sequence, heat transfer from the fluid to the inner tubing wall, conduction in the tubing wall, conduction in insulation (if any), natural convection and radiation within annulus, conduction in the casing wall and cement (Figure. 2.1). Since the thermal conductivities of tubing/casing wall

and cement, the film coefficients of flowing fluid can be determined with confidence, the difficulty lies in estimating convective and radiative heat transfer coefficient in the annulus and the thermal conductivity of insulation. In Willhite's paper, he used Stefan-Boltzmann law to calculate the radiative heat transfer coefficient, and the convective heat transfer coefficient is calculated from correlations obtained through an experiment on natural convection within two parallel vertical plates.

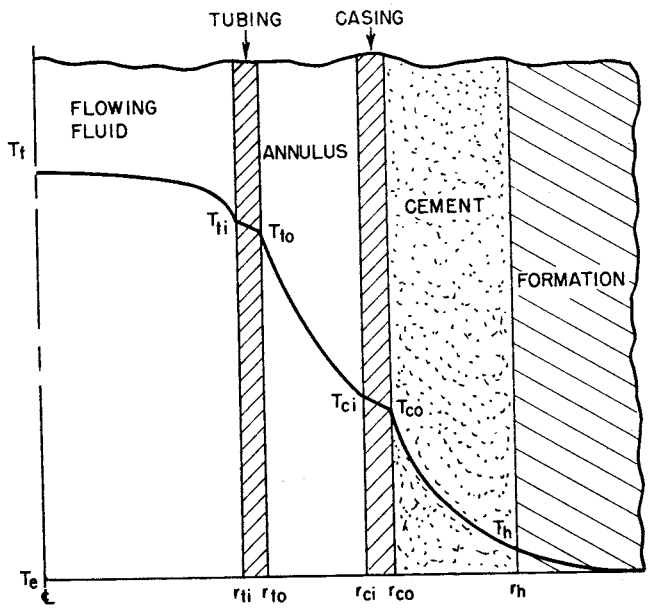

Fig. 1—Temperature distribution in an annular completion.

Figure 2.1: An illustration of Willhite's wellbore heat transfer model, subtracted from Willhite 1967 [65]

In 1972, Pacheco and Farouq Ali [49] formulated two differential equations to model wellbore steam injection and calculate steam pressure and quality. The model took into account the variation of steam temperature and pressure due to friction, as well as heat losses by radiation, conduction and convection. It was solved by numerical iteration. In 1981, Farouq Ali [20] extended his previous model [49]. The new pressure calculation took into account the slip and the prevailing flow regime using noted correlations. Heat loss was treated more rigorously by solving a conductive transfer equation, instead of using a time function. In 1982, Fontanilla and Aziz [22]

proposed two simultaneous ordinary differential equations for estimating steam pressure and quality. The major difference between this model and Farouq Ali's [20] is the correlations used to describe multiphase flow inside the wellbore tubing and the techniques used to simulate formation heat transfer.

In 1990 Wu and Pruess [67] proposed an analytical wellbore heat transfer model with various thermal properties in the surrounding formation layers. In 1994 Hasan and Kabir [25] proposed an analytical solution of flowing fluid temperature in wellbore tubing. Their model is based on a steady state energy balance equation that takes into account of the Joule-Thomson effect. The simplification of the original partial differential equation turned it into an ordinary differential equation that could be solved analytically with appropriate boundary conditions. The original model is further developed by the same author (Hasan, Kabir et al. 2003 [26]; Kabir, Hasan et al 2004 [32]; Hasan, Kabir et al. 2009 [27]). In 2010, Livescu et al. [44] developed a semi-analytical thermal multiphase wellbore model coupled to a reservoir model. The reservoir mass and energy balance equations coupled with wellbore mass and energy balance equations were solved numerically, with the suppliment of an analytical wellbore temperature solution.

In a series of papers by Bahonar et al, [4][5][6][7], he developed a numerical thermal multiphase wellbore simulator that solved the wellbore mass, momentum and energy balance equations in a fully implicit scheme. The wellbore model was then fully coupled to a 1D radial reservoir model and numerical results were validated against field data. In 2015, Xiong [69] improved Bahonar's model by introducing new correlations for wellbore annulus heat transfer. The new correlations enabled the wellbore model to handle different configurations and completions. The correlations for annulus heat transfer were obtained by a series of FLUENT simulations of buoyancy-driven flow in the annulus with different sizes, lengths and numbers of tubing.

2.2 Numerical Simulation of Natural Convection and Radiation

Natural convection in a confined space has been studied in great extend both experimentally and numerically. In fact, numerical simulation of natural convection has been a core problem in the subject of Computational Fluid Dynamics (CFD). When thermal wellbore models were first developed in 1960s, CFD techniques emerged and were only used in research by NASA. The development of CFD techniques relies on a combination of advances in computer power and algorithms. In 1970s finite-difference methods were proposed for Navier-Stokes equations. In 1980s finite volume methods were developed. In 1985 CFD techniques started to be applied to aeronautical engineering; in 1995, it was applied to "non-aero" industries [55]. Today the performance of current high-end servers has increased several thousand times, which allows CFD techniques to be applied more broadly.

A mathematical model of convective heat transfer is composed of a group of partial differential equations, i.e. the mass conservation equation, the momentum conservation equation(s) and the energy conservation equation, derived from the laws of *Conservation of Mass, Newton's Second Law of Motion* and *Conservation of Energy*. The model is solved either with *primary variables*, e.g. pressure, velocities and temperature, or with *secondary variables*, like the stream function, vorticity and temperature. The main difficulty with the primary variable methods lies in the proper discretization of pressure gradient and the coupling of pressure and velocities. Classical algorithms using primary variables include the SIMPLE algorithm series (SIMPLE, SIMPLER, SIMPLEC, SIMPLEX) developed by Spalding and Patankar [50].

The difficulties associated with the primary variable algorithms lead to the development of methods that eliminate the pressure terms from the governing equations. In a 2D problem, by cross differentiation of the two momentum equations, the pres-

sure terms are eliminated, producing a vorticity-transport equation. Combined with the definition of stream function, this forms the vorticity-stream function (secondary variables) approach.

Numerical studies of pure natural convection are numerous. In 1975, Kuehn and Goldstein [34] first studied the steady state natural convection in the annulus between horizontal concentric cylinders using experiments and numerical simulations. Two sets of experiments were run: one with air and the Rayleigh number up to 9.56×10^4, another with water and the Rayleigh number up to 9.76×10^5. The numerical study applied central difference along with Successive-Over-Relaxation (SOR) method to solve the vorticity-stream function based governing equations. The simulations support the experimental outcomes when comparing dimensionless temperature profile and local equivalent conductivity. In 1978, these two authors extended their experimental study to higher Rayleigh numbers and natural convection within eccentric horizontal cylindrical annuli [35]. Their study confirmed that with nitrogen (Pr=0.7) no steady flow pattern exists with high Rayleigh numbers, oscillations of the interferograms were first observed near $\mathrm{Ra}_L = 2 \times 10^5$.

de Vahl Davis and Thomas first studied the natural convection in isothermally heated vertical annuli and rectangular cavities [16] [62]. Many researchers then studied the same subject. Each author made an effort to extend the range of highest Rayleigh number and the aspect ratio. In 1982 Lee, Korpela and Horne [39] modelled the transient natural convection in a tall vertical annulus. They formed the governing equations in a manner that by setting the radius ratio to unity, the problem degenerates into rectangular cases. They observed multicellular convection in their numerical results with high aspect ratios. In 1983, Lee and Korpela [40] extended the study by comparing the numerical simulation of multicellular natural convection in a vertical slot with experiments results. Their calculated streamline faithfully represented what

has been seen in the laboratory showing smoke traces in air and particle trances in oils. They identified the limitation of accuracy of their numerical studies by pointing out the unreasonable jaggedness in the velocity profiles near the top and bottom boundaries.

A lot of discussion and development of numerical heat transfer focus on the discretization of convection terms in the governing equations. Although only first-order partial difference is involved in the convection term, its discretization is the most difficult to handle, due to the strong sign of direction associated with convection [58]. An appropriate format of convection term discretization determines the accuracy, stability and efficiency of the overall numerical algorithm. Since the common central-difference method fails when the Peclet number is high [57], remedies are invented for the difficulties encountered. Among these schemes a well-known one is the *upwind* scheme (more often referred as the *upstream* scheme in reservoir simulation). It was first proposed by Courant, Issacson and Rees [14]. The upwind scheme considers the flow direction to determine the discretization method and the interpolation/extrapolation value of the convected property at the grid cell interface. Other schemes that solve the problem associated with central difference are the exponential scheme [50], the hybrid scheme [11], and the power-law scheme [51]. However, Leonard [43] pointed out that these methods will cause false diffusion when Peclet number is high due to low truncation error (less than second-order). The *second-order upwind* scheme [41] inherits the merits of first order upwind scheme and reduces false diffusion. Moreover, the second-order upwind scheme is a conservative and absolute stable numerical scheme [57]. Other well-known higher order methods to avoid false diffusion include the third-order upwind scheme, and the QUICK [42] format. A thorough and detailed literature review on numerical heat transfer refers to Tao's book[57].

Most of the investigations neglect the contribution of radiative heat transfer. How-

ever, every object with a temperature greater than absolute zero can emit and absorb radiative (electromagnetic) energy. In engineering applications such as combustion, solar collector and nuclear engineering the influence of radiation on heat transfer cannot be neglected. This is very apparent in thermal recovery processes where studies have shown that radiation is high if the wellbore annulus contains a gas and the tubing is hot [19]. Huygen and Huitt [31] pointed out that radiative heat loss account for up to two thirds of the total wellbore heat loss when the annulus is dry.

In 1996, Weng and Chu [64] studied the steady state combined natural convection and volumetric radiation in a vertical annulus. They used the PROJECTION algorithms with primary variables and the two-dimensional P-1 approximation for the radiative transfer equation. In 1998, Kuo et al. [36] studied the transient combined natural convection and volumetric radiation within a horizontal annulus using spectral and finite volume prediction. Primary variable formulation and P-1 approximation for radiative transfer were also adopted in their study.

2.3 Vacuum-Insulated-Tubing (VIT) Heat Transfer Characteristics

Besides estimating wellbore heat loss, wellbore temperature control is critical to thermal well integrities, as high wellbore temperature may lead to annulus pressure build up and casing failures [21]. Vacuum insulated tubing (VIT) is now widely deployed in deepwater and arctic environments, however the design of a VIT installation introduces a number of considerations not present in a design using conventional tubings.

In 1983 Aeschliman [1] reported on the thermal efficiency of a steam injection well with insulated tubing in a steam flood pilot in the Aberfeldy Field near Lloydminster, Saskatchewan. It was observed that the coupling and internal structures (e.g. centralizers) accounted for up to half of the string heat loss when the annulus was

dry. For a wet annulus, casing temperature was maintained at 212 °F at all locations because of the steam generated at the hot couplings refluxing in the vented annulus.

In 2002 a series of three papers [10] [18] [23] addressed the failure of Well A-2 on the Marlin tension leg platform (TLP) located in the Gulf of Mexico. In the first paper, Bradford et. al [10] outlined several possible failure modes. By analytical and physical evidence, the primary failure mechanism is identified to be the incremental annulus fluid expansion (AFE) pressure in the annuli. Applying the failure analysis in the first paper, Ellis et al. [18] proposed a redesign process using VIT for the remaining Marlin wells. It was observed in the tests that heat loss at the coupling can dominate the performance of a VIT joint. In the third paper of the series, Gosch et al. [23] made a full-scale VIT testing with Fiber-optic cable run on completion to continuously monitor the production-annulus temperature profile. It was observed that natural convection significantly impacted VIT's ability to isolate tubing temperatures from the production annulus.

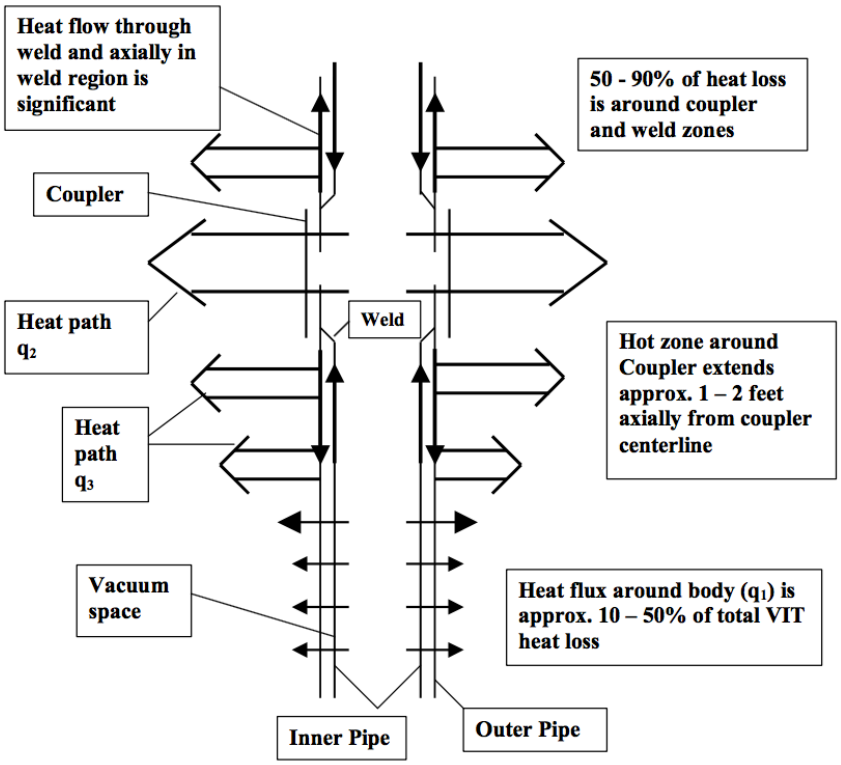

Figure 2.2: Three distinc paths of VIT heat transfer, subtracted from Azzola 2004 [2]

A VIT consists of two concentric joints of tubing welded together, where the annulus space between the two tubing is vacuum. Unlike conventional tubing, there are three different heat paths of a VIT [2]: the first path runs around the vacuum body (q_1 in Figure.2.2), the second path runs around the coupler (q_2 in Figure.2.2), and the third path runs axially along the inner pipe toward the weld, through the weld and axially down the outer pipe (q_3 in Figure.2.2). Both field data [23] and simulation studies [52][33] show that 50% to 90% heat loss is due to natural convection cells developed around the coupling area.

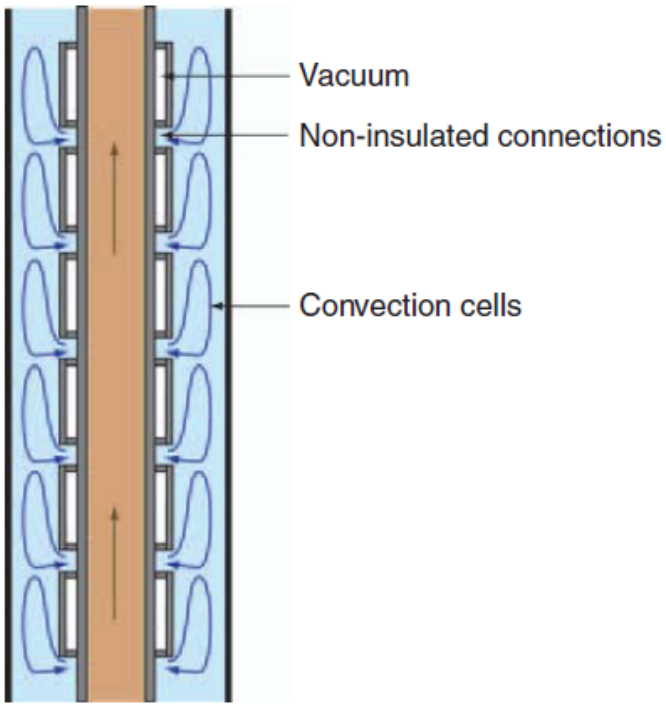

Figure 2.3: Major heat loss due to convection cells developed around the couplings, subtracted from Bellary 2009 [9]

Chapter 3

ANNULUS HEAT TRANSFER MODELING AND SIMULATION

In this chapter, the mathematical model of conjugate natural convection and radiation within a vertical concentric annulus space is elaborated. Both the primary variable formulation and the secondary variable formulation are derived. Details of numerical algorithms: the discretization, linearization, choice of linear solver and iteration scheme, are provided.

3.1 Mathematical Formulation

3.1.1 The Primary Variable Formulation

Consider a concentric vertical annular cavity of height l, inner radius r_i and outer radius r_o as shown in Fig.3.1. The inner wall is held at temperature T_i which is higher than the outer wall temperature T_o. The top and the bottom of the cavity are insulated. It is assumed that the Boussinesq approximation [24] is valid. Density in the gravitational force terms is represented by

$$\rho = \rho_o[1 - \alpha(T - T_o)] \tag{3.1- 1}$$

where ρ_o is the fluid density at temperature T_o, α is the thermal expansion coefficient.

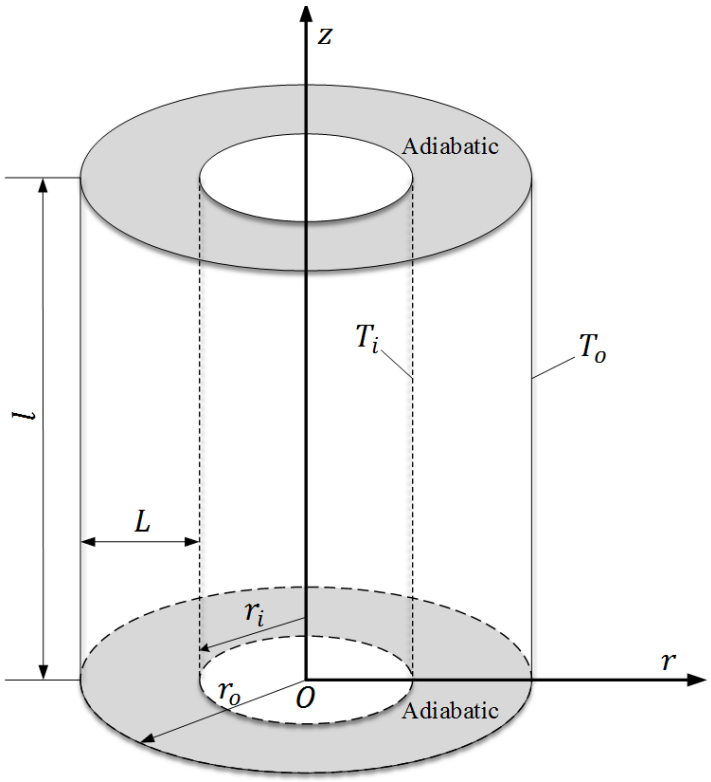

Figure 3.1: A schematic of vertical annulus

A cylindrical coordinate system is adopted, the equations governing the conservation of mass, momentum and energy, and the Radiative Transfer Equation (RTE) can be written in terms of the pressure p', velocities u', w', temperature T', and zero moment of intensity i_0. Let $L = r_o - r_i$ denote the gap width; let $H = l/L$ denote the aspect ratio; let $\kappa = r_i/r_o$ represent the radius ratio. Define $\kappa_l = (1-\kappa)/\kappa (= L/r_i)$, and $R = r\kappa_l + 1$. By introducing the following non-dimensional variables

$$
\begin{aligned}
&r = \frac{r' - r_i}{L}, \quad z = \frac{z'}{L}, \quad t = \frac{t'\nu}{L^2}, \\
&u = \frac{u' r_i}{\nu}, \quad w = \frac{w' r_i}{\nu}, \\
&T = \frac{T' - T_o}{T_i - T_o}, \quad p = \frac{p' r_i^2}{\rho \nu^2}, \quad I = \frac{i_0}{\sigma T_i^4},
\end{aligned}
\tag{3.1- 2}
$$

the governing equations take the form:

continuity:

$$\frac{\partial}{\partial r}(Ru) + \frac{\partial}{\partial z}(Rw) = 0 \tag{3.1- 3}$$

radial momentum:

$$\frac{\partial u}{\partial t} + \frac{1}{\mathrm{Pr}}\left(u\frac{\partial u}{\partial r} + w\frac{\partial u}{\partial z}\right) = -\frac{1}{\rho}\frac{\partial p}{\partial r} + \nabla^2 u - \frac{\kappa_l^2}{R^2}u \tag{3.1- 4}$$

axial momentum:

$$\frac{\partial w}{\partial t} + \frac{1}{\mathrm{Pr}}\left(u\frac{\partial w}{\partial r} + w\frac{\partial w}{\partial z}\right) = -\frac{1}{\rho}\frac{\partial p}{\partial z} + \nabla^2 w + \mathrm{Ra}T \tag{3.1- 5}$$

energy:

$$\frac{\partial T}{\partial t} + \frac{1}{\mathrm{Pr}}\left(u\frac{\partial T}{\partial r} + w\frac{\partial T}{\partial z}\right) = \frac{1}{\mathrm{Pr}}\nabla^2 T + \frac{1}{\mathrm{Pr}}\frac{T_f\tau_0^2}{N}\left(\left(\frac{T}{T_f}+1\right)^4 - I\right) \tag{3.1- 6}$$

and the radiative transfer equation:

$$\nabla^2 I = 3\tau_0^2\left(I - \left(\frac{T}{T_f}+1\right)^4\right) \tag{3.1- 7}$$

The P_1 differential approximation for a gray fluid [45] is used to model the radiative transfer. In the formulation, $\mathrm{Ra} = g\beta\Delta T L^3/\nu\alpha$ is the Rayleigh number; $\mathrm{Pr} = \nu/\alpha$ is the Prandtl number; and ν, α, β are the kinetic viscosity, thermal diffusivity and thermal expansion coefficient of the fluid. σ_a is the absorption coefficient, $\tau_0 = \sigma_a L$ is the optical thickness, $N = k\sigma_a/4\sigma T_i^3$ is the conduction-to-radiation parameter that indicate the relative importance of the radiation effect. ∇^2 is the Laplace operator:

$$\nabla^2 = \frac{\partial^2}{\partial r^2} + \frac{\kappa_l}{R}\frac{\partial}{\partial r} + \frac{\partial^2}{\partial z^2}. \tag{3.1- 8}$$

3.1.2 The Vorticity-Stream Function Formulation

The main difficulty with the primary variable methods lies in the proper discretization of pressure gradient and the coupling of pressure and velocities. Therefore methods that eliminate the pressure terms from the governing equations are developed. In a 2D problem, by cross differentiation of the two momentum equations, the pressure terms are eliminated, producing a vorticity-transport equation. Combined with the definition of stream function, this forms the vorticity-stream function (secondary variables) approach.

By differentiating Eq.3.1- 4 with respect to z and Eq. 3.1- 5 with respect to r and subtract one from the other, a vorticity-transfer equation is obtained with ζ as the dependent variable,

$$\frac{\partial \zeta}{\partial t} + \frac{1}{\mathrm{Pr}}\left(u\frac{\partial \zeta}{\partial r} + w\frac{\partial \zeta}{\partial z}\right) = \nabla^2\zeta + \frac{1}{\mathrm{Pr}}\frac{\kappa_l}{R}u\zeta - \frac{\kappa_l^2}{R^2}\zeta + \mathrm{Ra}\frac{\partial T}{\partial r}, \tag{3.1- 9}$$

where

$$\zeta \equiv -(\partial u/\partial z - \partial w/\partial r) \tag{3.1- 10}$$

is the non-dimensional vorticity. Physically, vorticity describes the local spinning motion of a continuum near the point under consideration.

The non-dimensional stream function ψ is defined by

$$\frac{1}{R}\frac{\partial \psi}{\partial z} = u, \quad \frac{1}{R}\frac{\partial \psi}{\partial r} = -w. \tag{3.1- 11}$$

It can be shown that ψ identically satisfy the continuity equation Eq.3.1- 3, and it relates to the vorticity by

$$\frac{1}{R}\left(\nabla^2\psi - \frac{2\kappa_l}{R}\frac{\partial \psi}{\partial r}\right) = -\zeta \tag{3.1- 12}$$

Therefore the governing equations with stream-function vorticity approach take the form:

$$\frac{\partial \zeta}{\partial t} + \frac{1}{\mathrm{Pr}}\left(u\frac{\partial \zeta}{\partial r} + w\frac{\partial \zeta}{\partial z}\right) = \nabla^2\zeta + \frac{1}{\mathrm{Pr}}\frac{\kappa_l}{R}u\zeta - \frac{\kappa_l^2}{R^2}\zeta + \mathrm{Ra}\frac{\partial T}{\partial r} \tag{3.1- 13}$$

$$\frac{1}{R}\left(\nabla^2\psi - \frac{2\kappa_l}{R}\frac{\partial \psi}{\partial r}\right) = -\zeta \tag{3.1- 14}$$

$$\frac{\partial T}{\partial t} + \frac{1}{\mathrm{Pr}}\left(u\frac{\partial T}{\partial r} + w\frac{\partial T}{\partial z}\right) = \frac{1}{\mathrm{Pr}}\nabla^2 T + \frac{1}{\mathrm{Pr}}\frac{T_f\tau_0^2}{N}\left(\left(\frac{T}{T_f}+1\right)^4 - I\right) \tag{3.1- 15}$$

$$\nabla^2 I = 3\tau_0^2\left(I - \left(\frac{T}{T_f}+1\right)^4\right) \tag{3.1- 16}$$

together with the definition of stream function ψ in Eq.3.1- 11 as the continuity equation.

3.1.3 Boundary Conditions

The boundary conditions are given by:

at inner cylinder wall $r = 0$,

$$\psi = 0, \quad u = w = 0, \tag{3.1- 17a}$$

$$\zeta = -\partial^2\psi/\partial r^2, \tag{3.1- 17b}$$

$$T = 1, \tag{3.1- 17c}$$

$$\left(1 - \frac{2}{3\tau_0}\frac{\partial}{\partial r}\right) I = \left(\frac{1}{T_f}+1\right)^4 \tag{3.1- 17d}$$

at outer cylinder wall $r = 1$,

$$\psi = 0, \quad u = w = 0, \tag{3.1- 18a}$$

$$\zeta = -\frac{1}{\kappa_l + 1}\frac{\partial^{\psi}}{\partial r^2}, \tag{3.1- 18b}$$

$$T = 0, \tag{3.1- 18c}$$

$$\left(1 + \frac{2}{3\tau_0}\frac{\partial}{\partial r}\right) I = 1 \tag{3.1- 18d}$$

at the bottom insulation wall $z = 0$,

$$\psi = 0, \quad u = w = 0, \tag{3.1- 19a}$$

$$\zeta = -\frac{1}{R}\frac{\partial^2 \psi}{\partial z^2}, \tag{3.1- 19b}$$

$$\frac{\partial T}{\partial z} + \frac{1}{3N}\frac{\partial I}{\partial z} = 0, \tag{3.1- 19c}$$

$$\left(1 - \frac{2}{3\tau_0}\frac{\partial}{\partial z}\right) I = \left(\frac{T}{T_f} + 1\right)^4 \tag{3.1- 19d}$$

at the top insulation wall $z = 1$,

$$\psi = 0, \quad u = w = 0, \tag{3.1- 20a}$$

$$\zeta = -\frac{1}{R}\frac{\partial^2 \psi}{\partial z^2}, \tag{3.1- 20b}$$

$$\frac{\partial T}{\partial z} + \frac{1}{3N}\frac{\partial I}{\partial z} = 0, \tag{3.1- 20c}$$

$$\left(1 + \frac{2}{3\tau_0}\frac{\partial}{\partial z}\right) I = \left(\frac{T}{T_f} + 1\right)^4 \tag{3.1- 20d}$$

Vorticity Boundary Conditions

Note that two sets of boundary conditions are given for stream function (as velocity boundaries are treated as Neumann boundary for stream function), but there are none for vorticity. In fact, one of the major difficulties in the vorticity-stream function approach is determining the numerical non-slip wall boundary conditions for vorticity. Failure of proper representation of the vorticity boundary creates challenges to achieve a converged solution [50]. This problem has been addressed by several papers ([66][30][56][46]) and continuous to be investigated in the Computational Fluid Dynamics (CFD) literature.

The stream-function vorticity formulation leads to two sets of boundary conditions for stream function, but there are for vorticity. According to the governing equation Eq.3.1- 14,

$$\begin{aligned}\zeta &= -\frac{1}{R}\left(\nabla^2\psi - \frac{2\kappa_l}{R}\frac{\partial\psi}{\partial r}\right) \\ &= -\frac{1}{R}\left(\frac{\partial^2\psi}{\partial r^2} + \frac{\kappa_l}{R}\frac{\partial\psi}{\partial r} + \frac{\partial^2\psi}{\partial^2 z}\right) - \frac{2\kappa_l}{R}\frac{\partial\psi}{\partial r}\end{aligned} \tag{3.1- 21}$$

the following boundary conditions for vorticity are derived:

at $r = 0$, since $\psi = 0, \partial\psi/\partial r = 0$, $\partial\psi/\partial z|_{r=0} = 0$, $\partial^2\psi/\partial z^2|_{r=0} = 0$, $R = 1$, thereby

$$\zeta = -\frac{1}{R}\frac{\partial^2\psi}{\partial r^2} = -\frac{\partial^2\psi}{\partial r^2} \tag{3.1- 22}$$

at $r = 1, R = \kappa_l + 1$, similarly,

$$\zeta = -\frac{1}{R}\frac{\partial^2\psi}{\partial r^2} = -\frac{1}{\kappa_l + 1}\frac{\partial^2\psi}{\partial r^2} \tag{3.1- 23}$$

at $z = 0$, since $\psi = 0$, we have $\partial\psi/\partial r|_{z=0} = 0$, and $\partial^2\psi/\partial r^2|_{z=0} = 0$, thereby

$$\zeta = -\frac{1}{R}\frac{\partial^2\psi}{\partial z^2} \tag{3.1- 24}$$

at $z = 1$, similarly,

$$\zeta = -\frac{1}{R}\frac{\partial^2\psi}{\partial z^2} \tag{3.1- 25}$$

As can be seen, the coupled nature of $\psi - \zeta$ is not only shown in the governing equations but also in the boundary conditions.

With the formulation of non-dimensional variables, pure natural convection can be simulated by setting $\tau_0 = 0$ hence Eq. 3.1- 16 vanishes. By further setting the radius ratio to one, calculations for the rectangular cases can be conducted.

3.2 Discretization Method

3.2.1 The Computational Domain

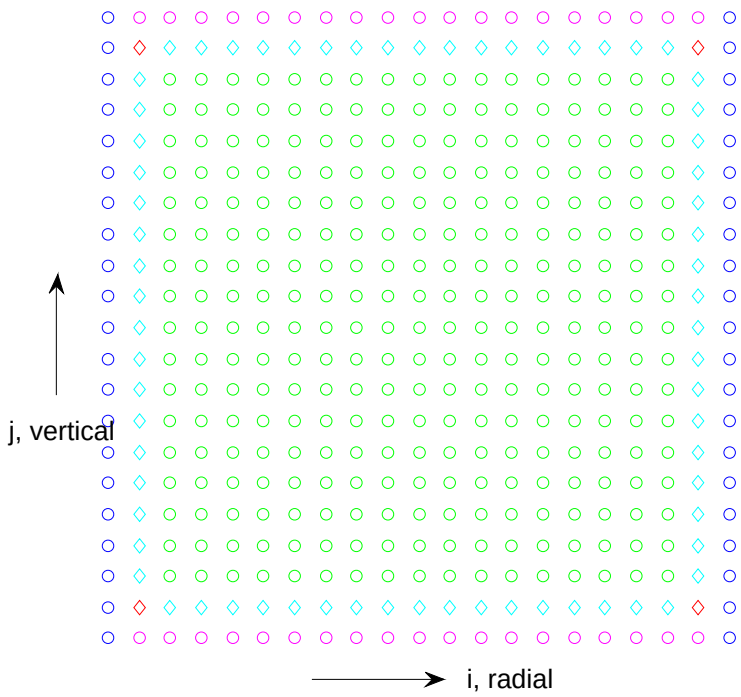

Figure 3.2: The computational domain

A point-distributed grid system is applied with Nmax nodes along the radial direction and Mmax nodes the axial direction, as shown in Figure.3.2. The grid size is uniform, with Δr in the radial direction, Δz in the axial direction. Control volume method is deployed to discretize the governing equations.

3.2.2 Discretization of the Diffusion Term

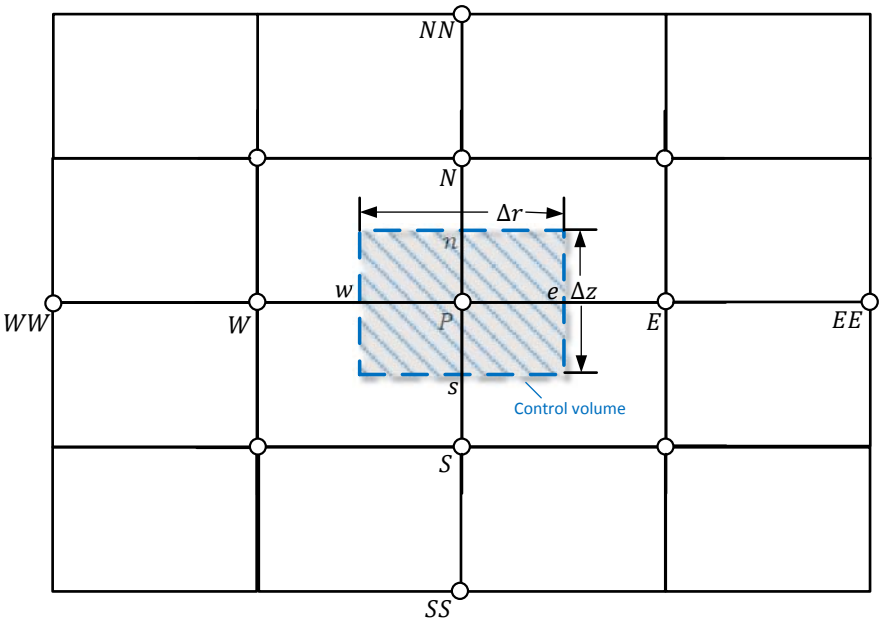

Figure 3.3: A sketch of a control volume

Take any arbitrary variable ϕ for example, the diffusion term $\nabla^2\phi$ is discretized by the standard second-order central difference scheme:

$$\mathscr{D}\nabla^2\phi = \frac{\phi_E - 2\phi_P + \phi_W}{\Delta r^2} + \frac{\kappa_l}{R}\frac{\phi_E - \phi_W}{2\Delta r} + \frac{\phi_N - 2\phi_P + \phi_S}{\Delta z^2} \tag{3.2- 1}$$

write

$$D_e = \frac{1}{\Delta r^2} + \frac{\kappa_l}{2R\Delta r} \tag{3.2- 2a}$$

$$D_w = \frac{1}{\Delta r^2} - \frac{\kappa_l}{2R\Delta r} \tag{3.2- 2b}$$

$$D_n = \frac{1}{\Delta z^2} \tag{3.2- 2c}$$

$$D_s = \frac{1}{\Delta z^2} \tag{3.2- 2d}$$

$$D_p = -2\frac{1}{\Delta r^2} - 2\frac{1}{\Delta z^2} \tag{3.2- 2e}$$

where $e, w, p, n,$ and s designate the location of the control surface of each control volume. Figure.3.3 gives a schematic explanation of the symbols used in Eqs. 3.2- 2. The discretization of diffusion term can be written as

$$\mathscr{D}\nabla^2\phi = (D_n, D_w, D_p, D_e, D_s) \begin{bmatrix} \phi_N \\ \phi_W \\ \phi_P \\ \phi_E \\ \phi_S \end{bmatrix} \tag{3.2- 3}$$

D_s, D_w, D_p, D_e and D_n are denoted as the *diffusion term coefficients*, and they can be written in a vector format $\boldsymbol{D} = (D_s, D_w, D_p, D_e, D_n)^T$. Next a vector $\boldsymbol{\phi}_5 = (\phi_S, \phi_W, \phi_P, \phi_E, \phi_N)^T$ is introduced and now the discretization of diffusion term can be represented succinctly by

$$\mathscr{D}\nabla^2\phi = \boldsymbol{D}^T\boldsymbol{\phi}_5. \tag{3.2- 4}$$

3.2.3 Discretization of the Convection Term

Using a finite volume approach, the first order derivative in the convection term $u\partial\phi/\partial r$ is approximated as

$$\mathscr{D}\left(u\frac{\partial\phi}{\partial r}\right) = \frac{u_e\phi_e - u_w\phi_w}{\Delta r}$$

Difference extrapolation methods for ϕ_e and ϕ_w lead to difference discretization scheme. In the present study, second-order upwind (SUS) scheme is selected for the discretization of convection terms. The second-order upwind scheme is a high-order, conservative and absolute stable scheme [57]. As illustrated in Figure. 3.4, the

second order upwind extrapolation of the value on finite volume surface is defined as

$$\phi_w = \begin{cases} 1.5\phi_W - 0.5\phi_{WW}, & u_w > 0 \\ 1.5\phi_P - 0.5\phi_E, & u_w < 0 \end{cases}$$

$$\phi_e = \begin{cases} 1.5\phi_P - 0.5\phi_W, & u_e > 0 \\ 1.5\phi_E - 0.5\phi_{EE}, & u_e < 0 \end{cases}$$

In a more compact form, the second order upwind scheme for convection terms can be approximated by

$$\begin{aligned} &\mathscr{D}\left(u\frac{\partial\phi}{\partial r}\right) = \frac{u_e}{\Delta r}\phi_e - \frac{u_w}{\Delta r}\phi_w \\ &= (1.5\phi_P - 0.5\phi_W)[\![u_e, 0]\!]/\Delta r - (1.5\phi_E - 0.5\phi_{EE})[\![-u_e, 0]\!]/\Delta r \\ &- (1.5\phi_W - 0.5\phi_{WW})[\![u_w, 0]\!]/\Delta r + (1.5\phi_P - 0.5\phi_E)[\![-u_w, 0]\!]/\Delta r \end{aligned} \tag{3.2- 5}$$

where $[\![a, b]\!] = \max(a, b)$.

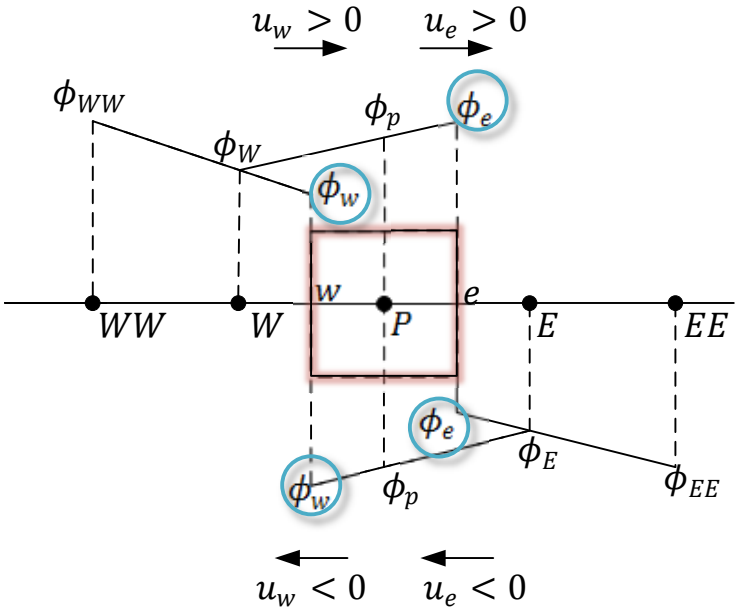

Figure 3.4: Second-order upwind scheme

Similarly in the axial direction,

$$\begin{aligned}\mathscr{D}\left(w\frac{\partial\phi}{\partial z}\right) &= \frac{w_n\phi_n - w_s\phi_s}{\Delta z} \\ &= (1.5\phi_P - 0.5\phi_S)[\![w_n, 0]\!]/\Delta z - (1.5\phi_N - 0.5\phi_{NN})[\![-w_n, 0]\!]/\Delta z \\ &- (1.5\phi_S - 0.5\phi_{SS})[\![w_s, 0]\!]/\Delta z + (1.5\phi_P - 0.5\phi_N)[\![-w_s, 0]\!]/\Delta z\end{aligned} \tag{3.2- 6}$$

The *convection term coefficients* are defined as

$$F_{SS} = 0.5[\![w_s, 0]\!]/\Delta z \tag{3.2- 7a}$$

$$F_S = -1.5[\![w_s, 0]\!]/\Delta z - 0.5[\![w_n, 0]\!]/\Delta z \tag{3.2- 7b}$$

$$F_{WW} = 0.5[\![u_w, 0]\!]/\Delta r \tag{3.2- 7c}$$

$$F_W = -0.5[\![u_e, 0]\!]/dr - 1.5[\![u_w, 0]\!]/\Delta r \tag{3.2- 7d}$$

$$F_P = 1.5[\![u_e, 0]\!]/\Delta r + 1.5[\![-u_w, 0]\!]/\Delta r + 1.5[\![w_n, 0]\!]/\Delta z + 1.5[\![-w_s, 0]\!]/\Delta z \tag{3.2- 7e}$$

$$F_E = -1.5[\![-u_e, 0]\!]/\Delta r - 0.5[\![-u_w, 0]\!]/\Delta r \tag{3.2- 7f}$$

$$F_{EE} = 0.5[\![-u_e, 0]\!]/\Delta r \tag{3.2- 7g}$$

$$F_N = -1.5[\![-w_n, 0]\!]/\Delta z - 0.5[\![-w_s, 0]\!]/\Delta z \tag{3.2- 7h}$$

$$F_{NN} = 0.5[\![-w_n, 0]\!]/\Delta z \tag{3.2- 7i}$$

and written in a vector format,

$$\boldsymbol{F} = (F_{SS}, F_S, F_{WW}, F_W, F_P, F_E, F_{EE}, F_N, F_{NN})^T.$$

The nine-point stencil can be written in a vector format,

$$\boldsymbol{\phi}_9 = (\phi_{SS}, \phi_S, \phi_{WW}, \phi_W, \phi_P, \phi_E, \phi_{EE}, \phi_N, \phi_{NN})^T,$$

thus the convection term discretization can be written succinctly as

$$\mathscr{D}\left(u\frac{\partial \phi}{\partial r} + w\frac{\partial \phi}{\partial z}\right) = \boldsymbol{F}^T\boldsymbol{\phi}_9 \tag{3.2- 8}$$

Since the formulated scheme results in a nine-point stencil in 2D mesh, as displayed in Figure 3.3, modifications must be made to accommodate control volumes adjacent to the boundaries. Details of the modifications are shown in Appendix A.

3.2.4 Discretization of Velocities

Velocities at each control volume face are needed to calculate the convection term coefficients, as shown in Eqs. 3.2- 7. They are discretized as follow:

$$u_w = \frac{1}{R}\frac{\psi_{sw} - \psi_{nw}}{\Delta r} = \frac{1}{R}\frac{\psi_S + \psi_{SW} - \psi_N - \psi_{NW}}{4\Delta r} \tag{3.2- 9a}$$

$$u_e = \frac{1}{R}\frac{\psi_{se} - \psi_{ne}}{\Delta r} = \frac{1}{R}\frac{\psi_S + \psi_{SE} - \psi_N - \psi_{NE}}{4\Delta r} \tag{3.2- 9b}$$

$$w_n = -\frac{1}{R}\frac{\psi_{ne} - \psi_{nw}}{\Delta z} = -\frac{1}{R}\frac{\psi_{NE} + \psi_E - \psi_{NW} - \psi_W}{4\Delta z} \tag{3.2- 9c}$$

$$w_s = -\frac{1}{R}\frac{\psi_{se} - \psi_{sw}}{\Delta z} = -\frac{\psi_{SE} + \psi_E - \psi_{SW} - \psi_W}{4\Delta z} \tag{3.2- 9d}$$

The notations used are illustrated in Figure 3.5.

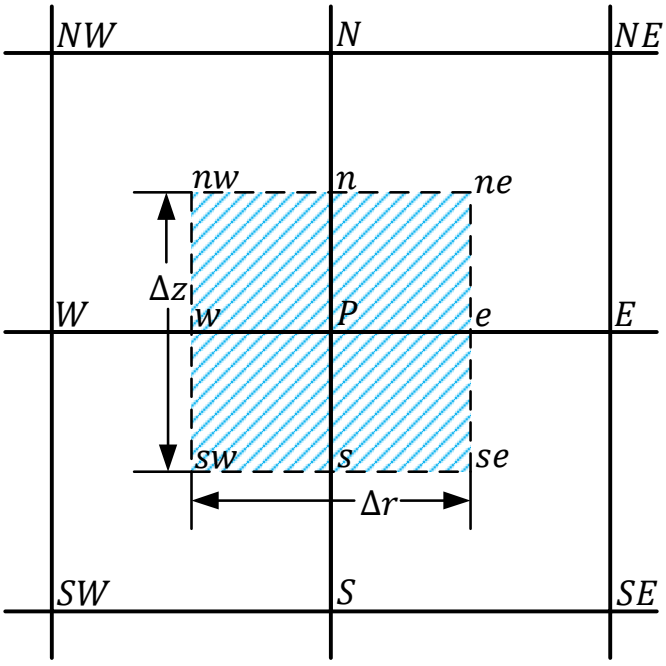

Figure 3.5: A sketch of notations

3.2.5 Discretization of Temporal Terms

Temporal terms are discretized by backward difference in order to make the formulation fully implicit. Using the notations introduced above, the discretized governing equations can be written as

$$\frac{\zeta_P^{n+1}-\zeta_P^n}{\Delta t}+\frac{1}{\mathrm{Pr}}\cdot(\mathbf{F}^{n+1})^T\cdot\boldsymbol{\zeta}_9^{n+1}-\mathbf{D}^T\cdot\boldsymbol{\zeta}_5^{n+1} = \frac{1}{\mathrm{Pr}}\frac{\kappa_l}{R}u^{n+1}\zeta_P^{n+1}-\frac{\kappa_l^2}{R^2}\zeta_P^{n+1}+Ra\frac{T_E^{n+1}-T_W^{n+1}}{2\Delta r} \tag{3.2- 10a}$$

$$\frac{1}{R}\mathbf{D}^T\cdot\boldsymbol{\psi}_5^{n+1}-\frac{\kappa_l}{R^2}\frac{\psi_E^{n+1}-\psi_W^{n+1}}{\Delta r}=-\zeta_P^{n+1} \tag{3.2- 10b}$$

$$\frac{T_P^{n+1}-T_P^n}{\Delta t}+\frac{1}{\mathrm{Pr}}\cdot(\mathbf{F}^{n+1})^T\cdot\mathbf{T}_9^{n+1}=\frac{1}{\mathrm{Pr}}\mathbf{D}^T\cdot\mathbf{T}_5^{n+1} + \frac{1}{\mathrm{Pr}}\frac{T_f\tau_0^2}{N}\left(\left(\frac{T_P^{n+1}}{T_f}+1\right)^4-I^{n+1}\right) \tag{3.2- 10c}$$

$$\mathbf{D}^T\cdot\mathbf{I}_5^{n+1}=3\tau_0^2\left(\left(I_P^{n+1}-\frac{T^{n+1}}{T_f}+1\right)^4\right) \tag{3.2- 10d}$$

3.2.6 Discretization of Boundary Conditions

As mentioned earlier in this chapter the vorticity boundary conditions need special attention. In this study Thom's formula [46] is applied to discretize the vorticity

boundary conditions:

$$\zeta_{0,j} = -\frac{2}{\Delta r^2}(\psi_{1,j} - \psi_{0,j}) = -\frac{2}{\Delta r^2}\psi_{1,j} \tag{3.2- 11a}$$

$$\zeta_{Nmax-1,j} = -\frac{2}{\Delta r^2(\kappa_l + 1)}(\psi_{Nmax-2,j} - \psi_{Nmax-1,j}) = -\frac{2}{\Delta r^2(\kappa_l + 1)}\psi_{Nmax-2,1} \tag{3.2- 11b}$$

$$\zeta_{i,0} = -\frac{2}{R\Delta z^2}(\psi_{i,1} - \psi_{i,0}) = -\frac{2}{R\Delta z^2}\psi_{i,1} \tag{3.2- 11c}$$

$$\zeta_{i,Mmax-1} = -\frac{2}{R\Delta z^2}(\psi_{i,Mmax-2} - \psi_{i,Mmax-1}) = -\frac{2}{R\Delta z^2}\psi_{i,Mmax-2} \tag{3.2- 11d}$$

Though this formula is first order accuracy, its relatively safe and won't lead to divergence in iterations [57].

3.3 Linearization and Solution Algorithm

The discretized algebraic systems Eqs.3.2- 10 are strongly coupled, and highly nonlinear in terms of convection term coefficients and the radiation terms in the energy balance equation as well as in RTE. To linearize, for each time step $n+1$, an inner iteration is introduced (superscript $n+1$ is omitted when not confusing):

$$\begin{aligned}&\frac{\zeta^{(\nu+1)}}{\Delta t} + \frac{1}{\mathrm{Pr}} \cdot (\mathbf{F}^{(\nu)})^T \cdot \boldsymbol{\zeta}_9^{(\nu+1)} - \mathbf{D}^T \cdot \boldsymbol{\zeta}_5^{(\nu+1)} - \frac{1}{\mathrm{Pr}}\frac{\kappa_l}{R}u^{(\nu)}\zeta^{(\nu+1)} + \frac{\kappa_l^2}{R^2}\zeta^{(\nu+1)} \\ &= \mathrm{Ra}\frac{T_E^{(\nu+1)} - T_W^{(\nu+1)}}{2\Delta r} + \frac{\zeta^n}{\Delta t}\end{aligned} \tag{3.3- 1}$$

$$\frac{1}{R}\mathbf{D}^T \cdot \boldsymbol{\psi}_5^{(\nu+1)} - \frac{\kappa_l}{R^2}\frac{\psi_E^{(\nu+1)} - \psi_W^{(\nu+1)}}{\Delta r} + \zeta^{(\nu+1)} = 0 \tag{3.3- 2}$$

$$\begin{aligned}&\frac{T^{(\nu+1)}}{\Delta t} + \frac{1}{\mathrm{Pr}} \cdot (\mathbf{F}^{(\nu)})^T \cdot \mathbf{T}_9^{(\nu+1)} - \frac{1}{\mathrm{Pr}}\mathbf{D}^T \cdot \mathbf{T}_5^{(\nu+1)} + \frac{1}{\mathrm{Pr}}\frac{T_f\tau_0^2}{N}I^{(\nu+1)} \\ &= \frac{1}{\mathrm{Pr}}\frac{T_f\tau_0^2}{N}\left(\frac{T^{(\nu+1)}}{T_f} + 1\right)^4 + \frac{T^n}{\Delta t}\end{aligned} \tag{3.3- 3}$$

$$\mathbf{D}^T \cdot \mathbf{I}_5^{(\nu+1)} - 3\tau_0^2 I^{(\nu+1)} = -3\tau_0^2 \left(\frac{T^{(\nu+1)}}{T_f} + 1 \right)^4 \tag{3.3- 4}$$

3.3.1 The Newton-Raphson Iteration

The wellbore annulus is usually filled with gaseous fluid, such as nitrogen or air, which has a very small absorption coefficient and thereby a very large conduction-to-radiation coefficient. On the other hand wellbore tubing in thermal recovery processes are usually very hot, up to 650 K. Thus the forth-order temperature term in both the energy balance equation and the RTE is intensively non-linear. In order to formulate an efficient scheme to cope with strong non-linearity, Newton-Raphson iteration method [12] is further embedded to solve the discretized energy equation Eq. 3.3- 3 and RTE Eq. 3.3- 4 fully implicitly. The Newton-Raphson iteration for energy balance equation and RTE can be written as:

$$\begin{aligned} &\frac{\delta T^{(l+1)}}{\Delta t} + \frac{1}{\mathrm{Pr}} \cdot (\mathbf{F}^{(\nu)})^T \cdot \delta \mathbf{T}_9^{(l+1)} - \frac{1}{\mathrm{Pr}} \mathbf{D}^T \cdot \delta \mathbf{T}_5^{(l+1)} + \frac{1}{\mathrm{Pr}} \frac{T_f \tau_0^2}{N} \delta I^{(l+1)} \\ &- \frac{1}{\mathrm{Pr}} \frac{\tau_0^2}{N} \cdot 4 \left(\frac{T^{(l)}}{T_f} + 1 \right)^3 \delta T^{(l+1)} = \frac{T^n}{\Delta t} - R_T(T^{(l)}, I^{(l)}) \end{aligned} \tag{3.3- 5}$$

where

$$\begin{aligned} R_T(T^{(l)}, I^{(l)}) &= \frac{\delta T^{(l)}}{\Delta t} + \frac{1}{\mathrm{Pr}} \cdot (\mathbf{F}^{(\nu)})^T \cdot \mathbf{T}_9^{(l)} - \frac{1}{\mathrm{Pr}} \mathbf{D}^T \cdot \mathbf{T}_5^{(l)} \\ &+ \frac{1}{\mathrm{Pr}} \frac{T_f \tau_0^2}{N} I^{(l)} - \frac{1}{\mathrm{Pr}} \frac{T_f \tau_0^2}{N} \cdot \left(\frac{T^{(l)}}{T_f} + 1 \right)^4 \end{aligned} \tag{3.3- 6}$$

and

$$\mathbf{D}^T \cdot \delta \mathbf{I}_5^{(l+1)} - 3\tau_0^2 \delta I^{(l+1)} + 3\tau_0^2 \cdot 4 \left(\frac{T^{(l)}}{T_f} + 1 \right)^3 \cdot \frac{\delta T^{(l+1)}}{T_f} = -R_I(T^{(l)}, I^{(l)}) \tag{3.3- 7}$$

where

$$R_I(T^{(l)}, I^{(l)}) = \mathbf{D}^T \cdot \mathbf{I}_5^{(l)} - 3\tau_0^2 I^{(l)} + 3\tau_0^2 \cdot \left(\frac{T^{(l)}}{T_f} + 1\right)^4 \tag{3.3- 8}$$

For temperature and intensity boundary conditions, similarly at inner cylinder wall $r = 0$,

$$\delta T^{(l+1)} = 1 - T^{(l)} \tag{3.3- 9}$$

$$\delta I_P^{(l+1)} - \frac{2}{3\tau_0}\frac{\delta I_E^{(l+1)} - \delta I_P^{(l+1)}}{\Delta r} = \left(\frac{1}{T_f} + 1\right)^4 - \left(I_P^{(l)} - \frac{2}{3\tau_0}\frac{I_E^{(l)} - I_P^{(l)}}{\Delta r}\right) \tag{3.3- 10}$$

at outer cylinder wall $r = 1$,

$$\delta T^{(l+1)} = 0 - T^{(l)} \tag{3.3- 11}$$

$$\delta I_P^{(l+1)} + \frac{2}{3\tau_0}\frac{\delta I_P^{(l+1)} - \delta I_W^{(l+1)}}{\Delta r} = 1 - \left(I_P^{(l)} + \frac{2}{3\tau_0}\frac{I_P^{(l)} - I_W^{(l)}}{\Delta r}\right) \tag{3.3- 12}$$

at bottom insulated wall $z = 0$,

$$(\delta T_N^{(l+1)} - \delta T_P^{(l+1)}) + \frac{1}{3N}(\delta I_N^{(l+1)} - \delta I_P^{(l+1)}) = -\left[(T_N^{(l)} - T_P^{(l)}) + \frac{1}{3N}(I_N^{(l)} - I_P^{(l)})\right] \tag{3.3- 13}$$

$$\begin{aligned} &\delta I_P^{(l+1)} - \frac{2}{3\tau_0}\frac{\delta I_N^{(l+1)} - \delta I_P^{(l+1)}}{\Delta z} - 4\left(\frac{T_P^{(l)}}{T_f} + 1\right)^3 \frac{\delta T^{(l+1)}}{T_f} \\ &= -\left[I_P^{(l)} - \frac{2}{3\tau_0}\frac{I_N^{(l)} - I_P^{(l)}}{dz} - \left(\frac{T_P^{(l)}}{T_f} + 1\right)^4\right] \end{aligned} \tag{3.3- 14}$$

at top insulated wall $z = H$,

$$(\delta T_P^{(l+1)} - \delta T_S^{(l+1)}) + \frac{1}{3N}(\delta I_P^{(l+1)} - \delta I_S^{(l+1)}) = -\left[(T_P^{(l)} - T_S^{(l)}) + \frac{1}{3N}(I_P^{(l)} - I_S^{(l)})\right] \tag{3.3- 15}$$

$$\begin{aligned} &\delta I_P^{(l+1)} + \frac{2}{3\tau_0}\frac{\delta I_P^{(l+1)} - \delta I_S^{(l+1)}}{\Delta z} - 4\left(\frac{T_P^{(l)}}{T_f} + 1\right)^3 \frac{\delta T^{(l+1)}}{T_f} \\ &= -\left[I_P^{(l)} + \frac{2}{3\tau_0}\frac{I_P^{(l)} - I_S^{(l)}}{dz} - \left(\frac{T_P^{(l)}}{T_f} + 1\right)^4\right] \end{aligned} \tag{3.3- 16}$$

Eq.3.3- 5 to Eq.3.3- 16 form a complete linear system in δT and δI. These equations are solved iteratively to update T and I till δT and δI become sufficiently small (1E-07 in this study).

3.3.2 The Overall Solution Algorithm

Assuming that solutions for time step n are known, then for time step $n+1$, assume $u^{(0)} = u^n$, $w^{(0)} = w^n$, $T^{(0)} = T^n$ and initiate the following iteration:

1. Assume $u^{(\nu)}, w^{(\nu)}, T^{(\nu)} = T^n$ and $I^{(\nu)}$ are already known, for inner iteration step $(\nu + 1)$:

2. Call Newton-Raphson iteration Eq.3.3- 5 Eq. 3.3- 7 to solve for $T^{(\nu+1)}$ and $I^{(\nu+1)}$. The systems for δT and δI are solved in a coupled manner.

3. With $T^{(\nu+1)}$ known, solve Eq.3.3- 1 and Eq.3.3- 2 in a coupled manner. The system becomes linear in $\zeta^{(\nu+1)}$ and $\psi^{(\nu+1)}$.

4. $\nu+ = 1$.

5. Repeat step 2-4, computation for time step $n+1$ completes when

$$|\phi^{(\nu+1)}, \phi^{(\nu)}|_{\max} \leq 10^{-7},$$

for $\phi = T, \psi, \zeta$.

6. The above-described solution algorithm is repeated until a steady state convergence criterion of the following form is met for all variables $\phi = T, \psi, \zeta$:

$$\frac{|\phi^{n+1} - \phi^{n}|_{\max}}{|\phi^{n+1}|_{\max}} \leq 10^{-6}.$$

7. The local Nusselt number along the inner and outer annulus walls are defined as

$$\mathrm{Nu} = \mathrm{Nu}_c + \mathrm{Nu}_r = -R\left(\frac{\partial T}{\partial r} + \frac{1}{3N}\frac{\partial I}{\partial r}\right) \qquad (3.3\text{- }17)$$

Numerical Nusselt numbers along the annulus walls is calculated using three grid points by the following formula:

$$\mathrm{Nu}_i = \frac{7T_{0,j} - 8T_{1,j} + 2T_{2,j}}{6\Delta r - 2\kappa_l(\Delta r)^2} + \frac{1}{3N}\frac{7I_{0,j} - 8I_{1,j} + 2I_{2,j}}{6\Delta r - 2\kappa_l(\Delta r)^2}, \qquad (3.3\text{- }18)$$

$$\begin{aligned}\mathrm{Nu}_o =& R\frac{7T_{Nmax-3,j} - 8T_{Nmax-2,j} + 2T_{Nmax-1,j}}{6\Delta r - 2\kappa_l(\Delta r)^2} \\ &+ \frac{1}{3N}\frac{7I_{Nmax-3,j} - 8I_{Nmax-2,j} + 2I_{Nmax-1,j}}{6\Delta r - 2\kappa_l(\Delta r)^2}.\end{aligned} \qquad (3.3\text{- }19)$$

8. The average Nusselt number can be defined as follows:

$$\overline{\mathrm{Nu}} = \frac{1}{H}\int_0^H \mathrm{Nu}\ \mathrm{d}z \qquad (3.3\text{- }20)$$

where numerical integrate is calculated using Simpson's rule.

9. The average heat loss rate of the inner cylinder wall per unit length is calculated by

$$\overline{Q_{loss}} = \frac{\overline{\mathrm{Nu}_i} \cdot k}{L \cdot (T_i - T_o) \cdot 2\pi r_i}. \qquad (3.3\text{- }21)$$

3.4 Solution of Linear Algebraic System of Equations

Discretization of high dimensional transport equations usually results in large, sparse and non-symmetric linear algebraic systems. Some of the widely used robust iterative methods includes: conjugate gradient method (CG), bi-conjugate gradient method (BiCG), bi-conjugate gradient stabilized method (Bi-CGSTAB), and the generalized minimal residual method (GMRES) [8]. The CG method is extremely effective when the coefficient matrix is symmetric positive definite. BiCG, like CG, uses limited storage. It can be deployed when the coefficient matrix is non-symmetric and nonsingular, however convergence is not always insured. BiCG-STAB is an enhancement of BiCG method, It has better convergence performance and saves computational time. However it may fail when the matrix is too large. In the present study, GMRES is deployed as the linear solver for its efficiency for general non-symmetric matrices [13]. Since it requires a large amount of storage, the restart version of GMRES is used. The incomplete LU fractorization algorithm is used as a preconditioning procedure for GMRES. An open source iterative linear solver library IML++ [47] is embedded in the program. The open source library SparseLib++ [48] is used for matrix operations.

3.5 Overall Algorithm

The overall numerical solution algorithm is summarized in the following flow chart (Figure.3.6).

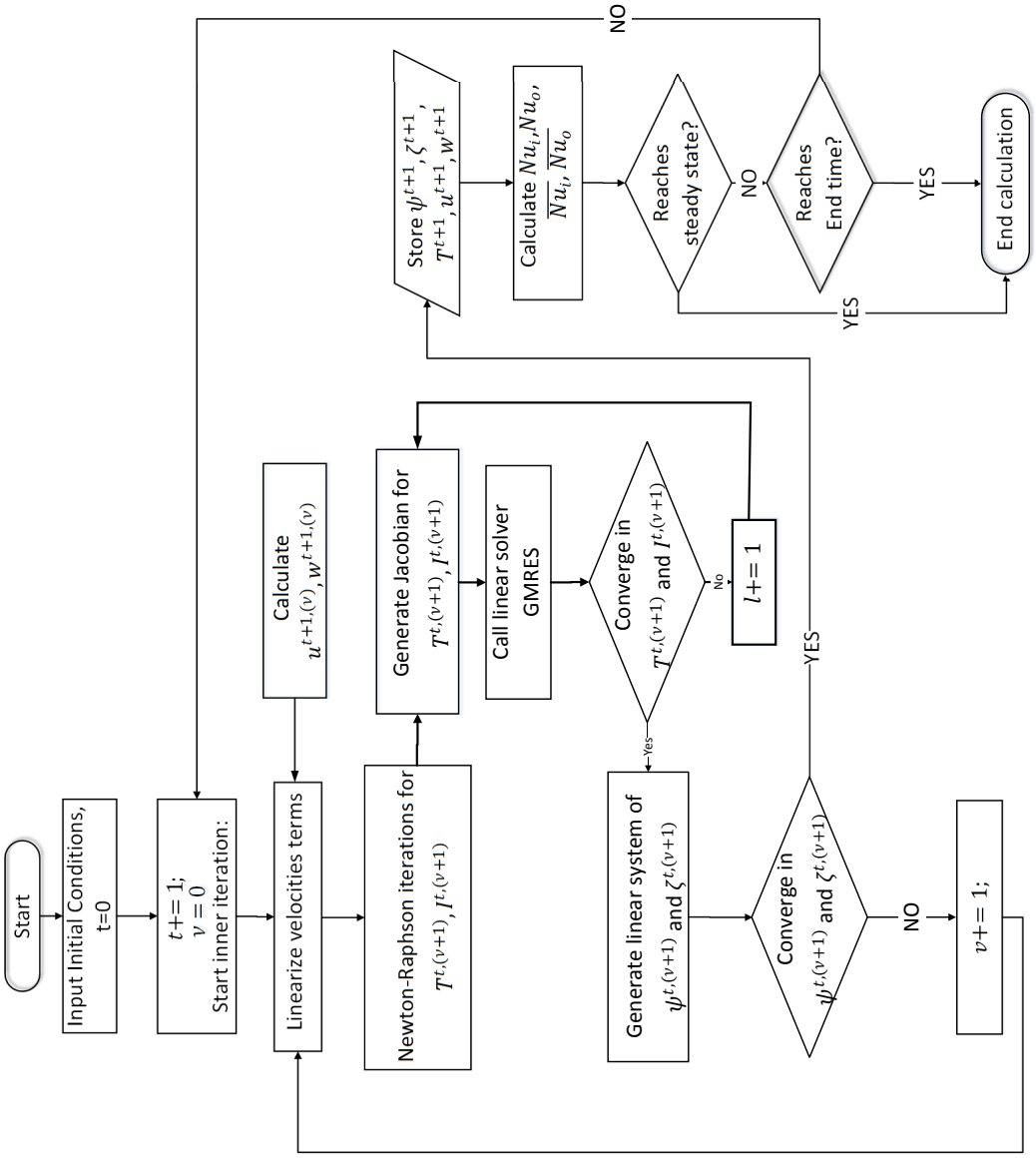

Figure 3.6: Flowchart of the calculation procedure

The program is developed in C++, for its merits of objective-oriented programming (OOP). It facilitates developing and maintaining large software systems, and

I/O management with other wellbore/reservoir simulators. The IDE used for software development is Microsoft Visual Studio 2013. A snapshot is shown in Figure. 3.7.

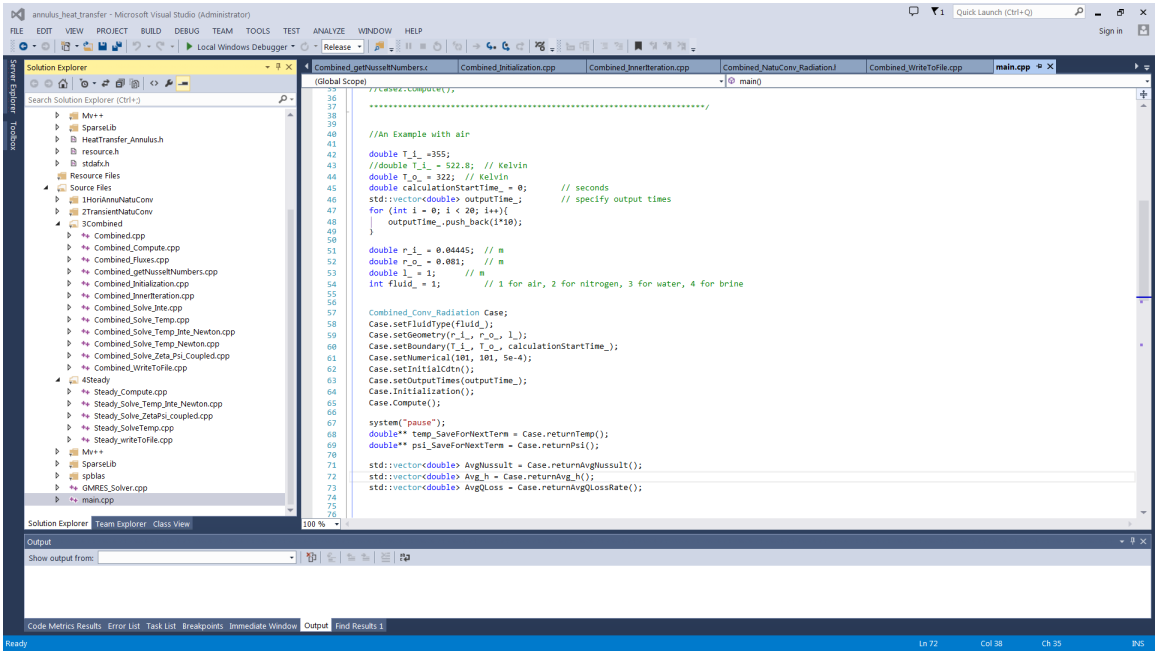

Figure 3.7: A snapshot of the program code

Chapter 4

MODEL VALIDATION AND SIMULATION RESULTS

In Chapter 3, the problem was formulated in a way such that by setting the radius ratio $\kappa = 1$ and the conduction-to-radiation coefficient $N = \infty$, the problem degenerates to pure natural convection in a vertical slot. In this Chapter, the numerical algorithm is first validated by comparing simulation results of pure convection in a square slot with literature outcomes. Subsequently, the effect of aspect ratio, radius ratio, conduction-to-radiation coefficient and dimensionless time, on the flow structure and heat transfer characteristics are examined.

4.1 Validation Tests

From the foregoing mathematical formulation, it can be seen that the flow field and temperature distribution for the problem under consideration are governed by the following dimensionless parameters: the Rayleigh number Ra, the Prandtl number Pr, the aspect ratio H, the radius ratio κ, the conduction-to-radiation parameter N and the optical thickness τ_0. In this chapter, in order to examine the main features of the interaction between natural convection and radiation, all computations are carried out with $\mathrm{Pr} = 0.7$ and $\tau_0 = 1$.

Validation tests are first performed for with $H = 1, \kappa = 1$, and $N = \infty$, corresponding to pure natural convection within a square slot. This setting allows the comparison of the present simulation results to numerous results found in the literature. Steady state simulation results have been obtained for $\mathrm{Ra} = 10^3 - 10^7$.

A mesh system of 41 (r direction) by (41 z direction) is found to be adequate for $\mathrm{Ra} = 10^3 - 10^5$, a 61×61 mesh for $\mathrm{Ra} = 10^6$, and a 101×101 mesh for $\mathrm{Ra} = 10^7$. The mesh system adopted is based on a series of grid-independence calculations using various meshes of $31 \times 31, 41 \times 41, 51 \times 51, 61 \times 61, 71 \times 71, 81 \times 81, 91 \times 91, 101 \times 101$.

Table 4.1: Comparison of present simulation results with other work

Ra	10^3	10^4	10^5	10^6	10^7
de Vahl Davis [15]					
$\overline{\mathrm{Nu}_i}$	1.118	2.243	4.519	8.800	-
$u_{\max}(1/2, z)$	3.649	16.1841	34.73	64.63	-
$w_{\max}(r, 1/2)$	3.697	19.6204	68.59	219.36	-
Le Quéré and Alziary de Roquefort [38][a] and Le Quéré [37][b]					
$\overline{\mathrm{Nu}_i}$	1.117[a]	2.245[a]	4.526[a]	8.825[b]	16.523[b]
$u_{\max}(1/2, z)$	3.6794[a]	16.183[a]	34.75[a]	64.83[b]	148.8[b]
$w_{\max}(r, 1/2)$	3.6974[a]	19.629[a]	68.85[a]	220.57[b]	699.3[b]
Ho and Lin[28]					
$\overline{\mathrm{Nu}_i}$	1.118	2.248	4.528	8.824	16.524
$u_{\max}(1/2, z)$	3.643	16.176	34.75	64.83	151.6
$w_{\max}(r, 1/2)$	3.697	19.628	68.63	219.86	705.3
Present study					
$\overline{\mathrm{Nu}_i}$	1.117	2.246	4.551	8.962	16.796
$u_{\max}(1/2, z)$	3.647	16.243	35.82	69.65	162.7
$w_{\max}(r, 1/2)$	3.694	19.522	66.87	216.36	692.4

Table 4.1 compares the steady state computation results with those of the benchmark solutions in the literature[15] [38][37][28], in terms of the average Nusselt number of inner cylinder wall, and the maximum velocity at both the horizontal and vertical mid-plane. It can be seen that the results of present simulations agree remarkably well with the benchmark results. This clearly confirms the validity of the present algorithm. In particular, the agreement is strong between the average Nu of the present study and the literature, as shown by a more intuitive comparison in Figure 4.1,

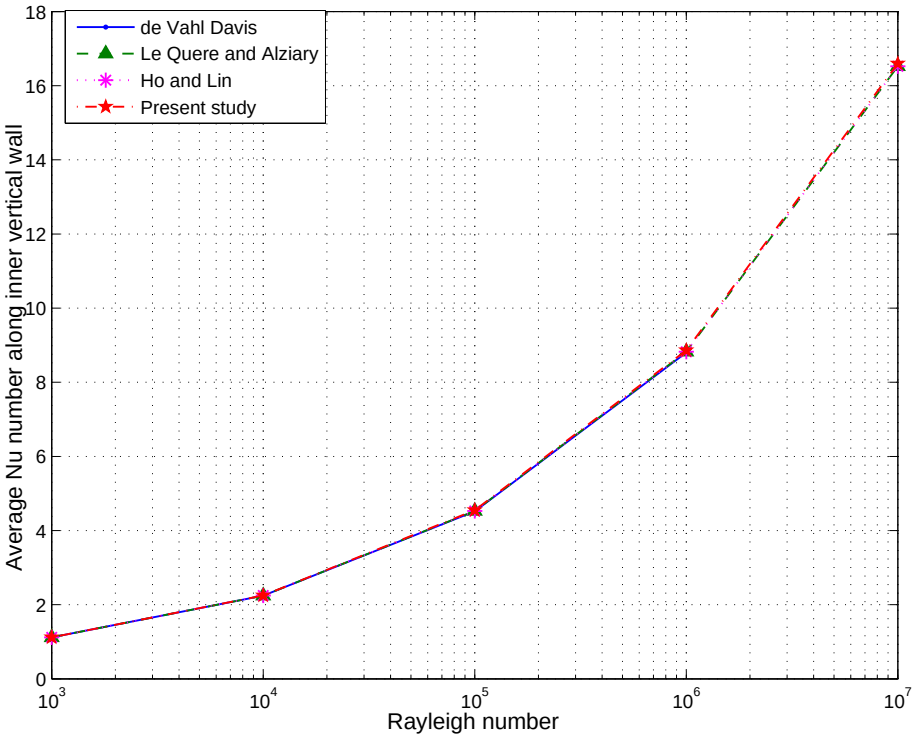

Figure 4.1: Comparison of average Nusselt number along inner vertical wall of present simulations and benchmark results

Figure 4.2 and 4.3 plot the (dimensionless) temperature and stream function as well as velocity field of the two-dimensional solutions obtained for $\mathrm{Ra} = 10^3 - 10^7$. In both figures, the centro-symmetry of the isotherms and streamlines can be detected. Moreover, the continuity shown in the velocity field plots also confirms the validity of the developed algorithm. By comparing the isotherms and stream lines, the Rayleigh number increases and the flow regime transits from nearly conduction to partially turbulent, which is in agreement with the benchmark results. For large Rayleigh numbers $\mathrm{Ra} = 10^6$ and 10^7, the flow structure and temperature distribution are featured by thin boundary layers along the vertical walls and secondary vortices in a thermally stratified core. In particular, the occurrence of a recirculation region and a flow divergence in the upper left and lower right corners of the enclosure at $\mathrm{Ra} = 10^7$ can be readily detected from the stream function plot in Figure.4.3.

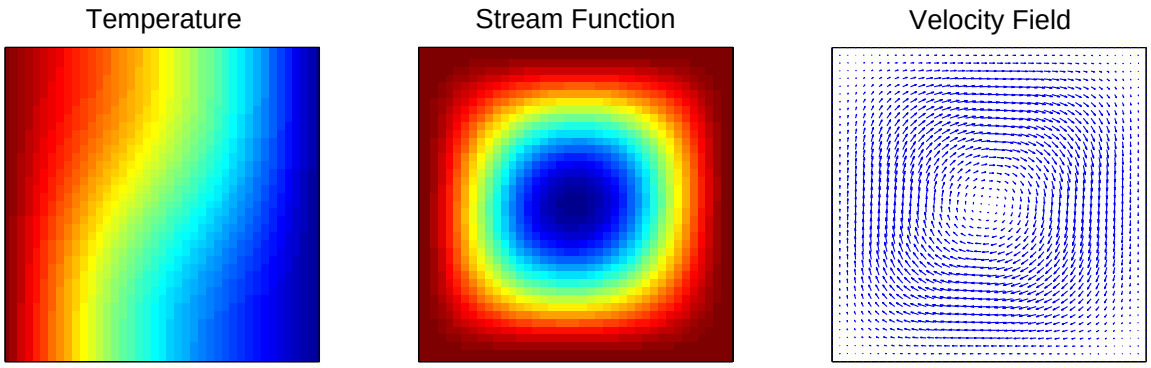

(a)

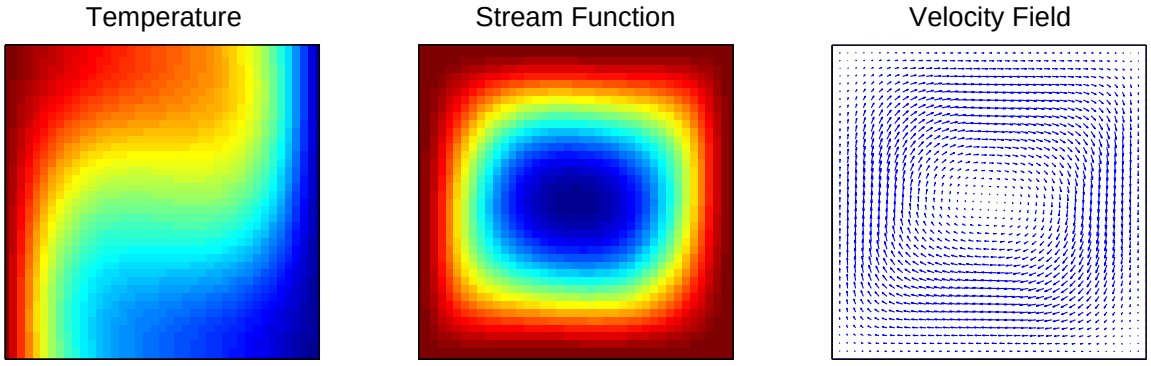

(b)

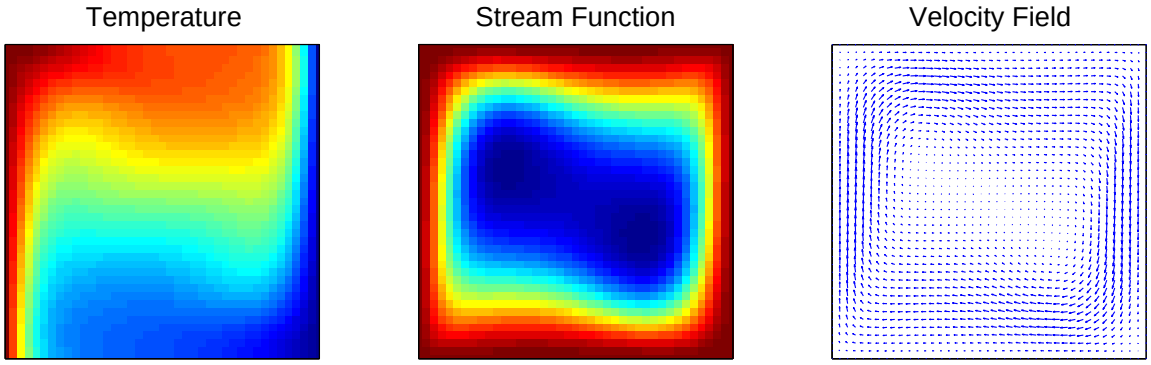

(c)

Figure 4.2: Plots of temperatures, stream functions and velocity fields for (a) $\mathrm{Ra} = 10^3$, (b) $\mathrm{Ra} = 10^4$ (c) $\mathrm{Ra} = 10^5$, with a 41×41 mesh

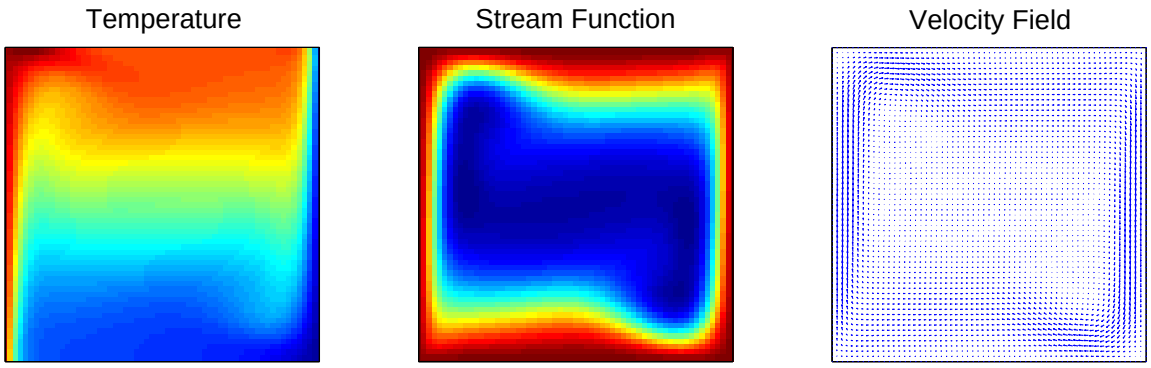

(a)

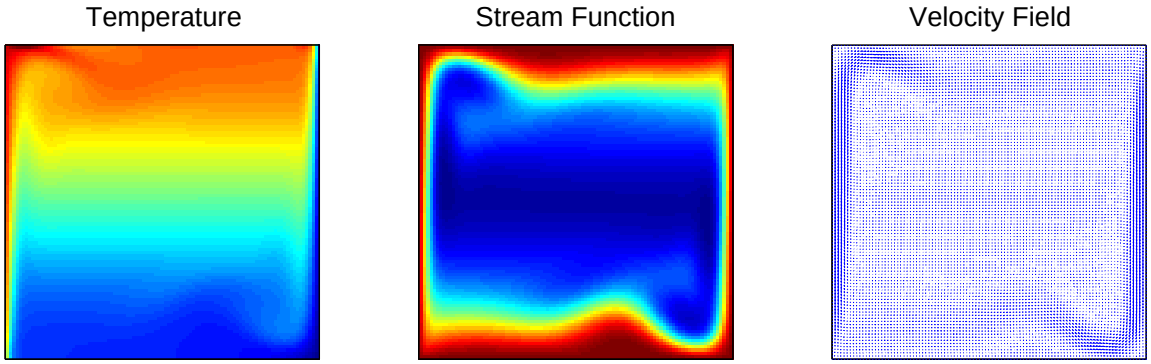

(b)

Figure 4.3: Plots of temperatures, stream functions and velocity fields for (a) $\mathrm{Ra} = 10^6$, with a 61×61 mesh (b) $\mathrm{Ra} = 10^7$, with a 101×101 mesh

4.2 Effect of Aspect Ratio, Radius Ratio and Radiation on the Flow Structure and Heat Transfer Characteristics

In the previous section, the effect of Rayleigh number on the flow structure and heat transfer characteristics of the problem under consideration has been clearly demonstrated in the validation tests. In this section, a total number of 20 simulations are run to examine the effect of aspect ratio, radius ratio and conduction-to-radiation coefficient on the flow field and heat transfer characteristics within the annulus. Parameters of each simulation are summarized in Table 4.2. Average Nusselt number along inner cylinder wall of each simulation is also presented in the table.

Table 4.2: A Summary of parameters used in simulations to examine the effects of aspect ratio, radius ratio and radiation

Case No.	Ra	Aspect ratio	Radius ratio	N	t	$\overline{\mathrm{Nu}_0}$
1	10^6	2	0.5	∞	steady state	10.564
2	10^6	4	0.5	∞	steady state	9.379
3	10^6	8	0.5	∞	steady state	8.165
4	10^6	10	0.5	∞	steady state	7.759
5	10^6	2	0.5	1	steady state	12.591
6	10^6	4	0.5	1	steady state	11.461
7	10^6	8	0.5	1	steady state	10.511
8	10^6	10	0.5	1	steady state	10.169
9	10^5	2	0.5	1	steady state	7.803
10	10^5	4	0.5	1	steady state	7.270
11	10^5	8	0.5	1	steady state	6.627
12	10^5	10	0.5	1	steady state	6.423
13	10^6	4	0.8	1	steady state	9.521
14	10^6	4	0.5	1	steady state	11.461
15	10^6	4	0.2	1	steady state	14.563
16	10^6	4	0.1	1	steady state	17.162
17	10^6	4	0.8	10	steady state	7.910
18	10^6	4	0.5	10	steady state	9.528
19	10^6	4	0.2	10	steady state	12.203
20	10^6	4	0.1	10	steady state	14.538

4.2.1 Effect of Aspect Ratio

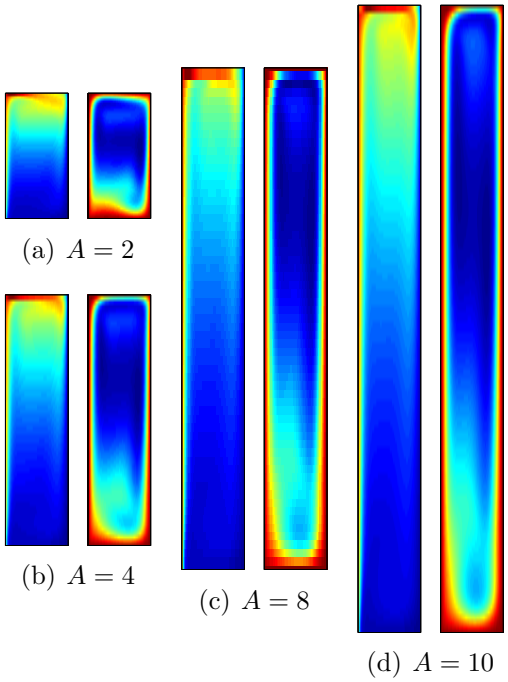

Figure 4.4: The effect of aspect ratio on the isotherms and streamlines for $\mathrm{Ra} = 10^6$ and $\kappa = 0.5$ without radiation, case No.1 - 4

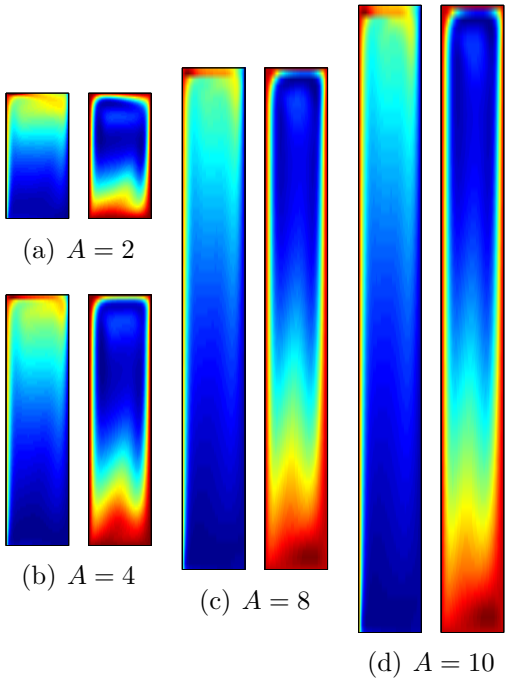

Figure 4.5: The effect of aspect ratio on the isotherms and streamlines for $\mathrm{Ra} = 10^6, \kappa = 0.5$, and $N = 1$, case No. 5-8

Figure 4.4 shows the effect of aspect ratio on the dimensionless isotherms and streamlines with $\mathrm{Ra} = 10^6, \kappa = 0.5$ and $N = \infty$. In each group of plots, the isotherm is displayed on the left and streamline on the right. Laminar convection is the primary heat transfer mode. Thermal boundary layer is observed near both walls for all aspect ratios. For $H = 2$, the isotherms in the center of the plane are almost flat; when the aspect ratio increases, isotherm inversion is more intensive, since the boundary layer is more readily developed for large aspect ratios. Figure 4.5 displays a corresponding group of simulations with the same parameters, except that the conduction-to-radiation coefficient is 1, indicating the effect of radiation. Comparing to Figure 4.5, the streamlines in Figure 4.5 are more uniform. Thus we conclude that radiation helps stabilize the flow structure.

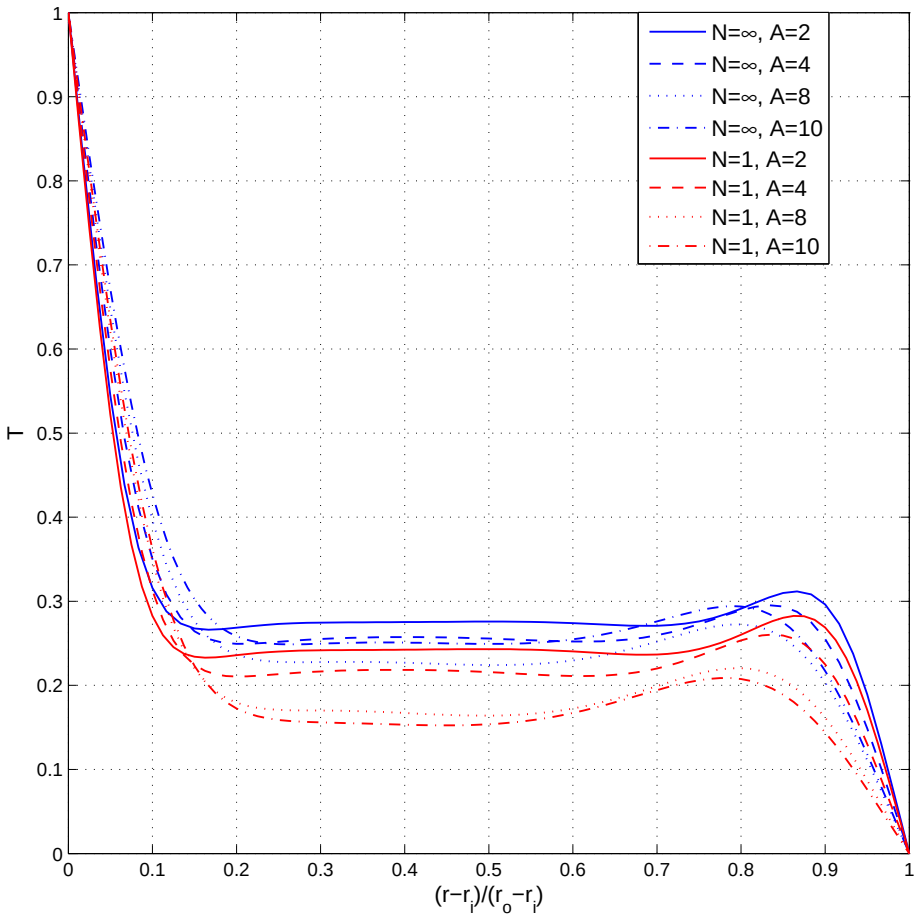

Figure 4.6: The effect of aspect ratio on the temperature profile at $z = 0.5H$, with $\mathrm{Ra} = 10^6$, $\kappa = 0.5$, for $N = \infty$ and 1

Figure 4.6 illustrates the effect of aspect ratio on the temperature profile at the horizontal mid-plane, with $\mathrm{Ra} = 10^6$, $\kappa = 0.5$, $N = \infty$ and 1. For a fixed aspect ratio, the temperature is higher in the pure convection scenario, i.e. $N = \infty$ than when $N = 1$. For a fixed N, the absolute value of the temperature gradient near both walls decreases as the aspect ratio increases. This phenomenon is because the thermal boundary layer is thicker when aspect ratio is large.

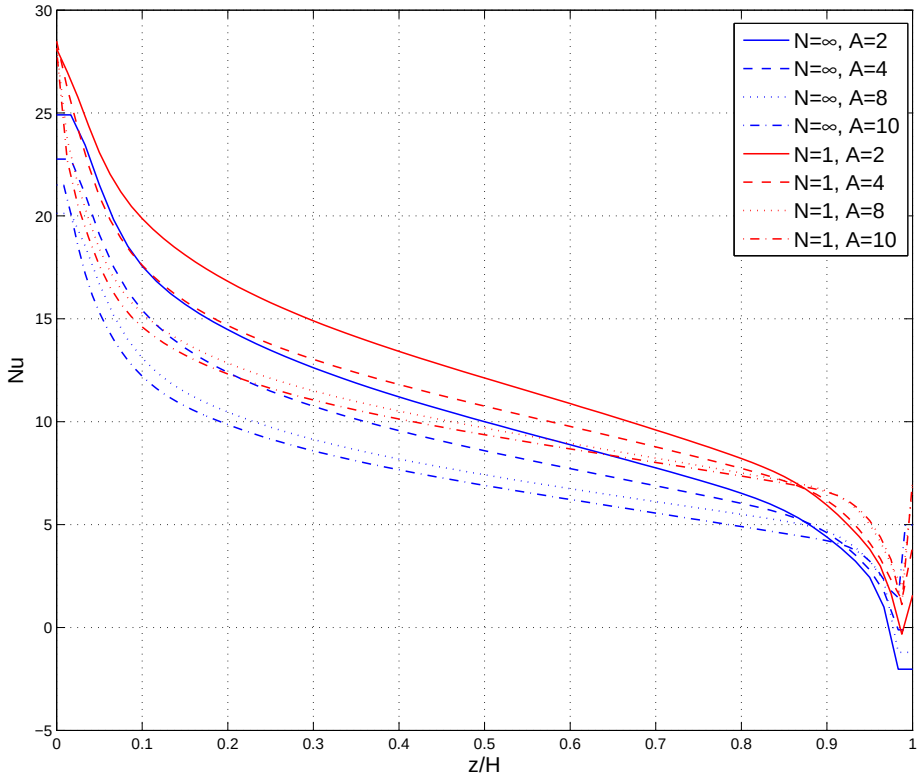

Figure 4.7: The effect of aspect ratio on local Nusselt number along the inner annulus wall at $\mathrm{Ra} = 10^6, \kappa = 0.5$, for $N = \infty$ and 1

Local Nusselt number along inner cylinder wall of each case discussed are shown in Figure 4.7. Local Nusselt numbers are higher when $N = 1$ than $N = \infty$, which is due to the contribution of radiation to the over all heat transfer rate. For a fixed N the local Nusselt number decreases as aspect ratio increases. Once again, this phenomenon can be explained by the fact that thermal boundary layer is more readily developed at large aspect ratios.

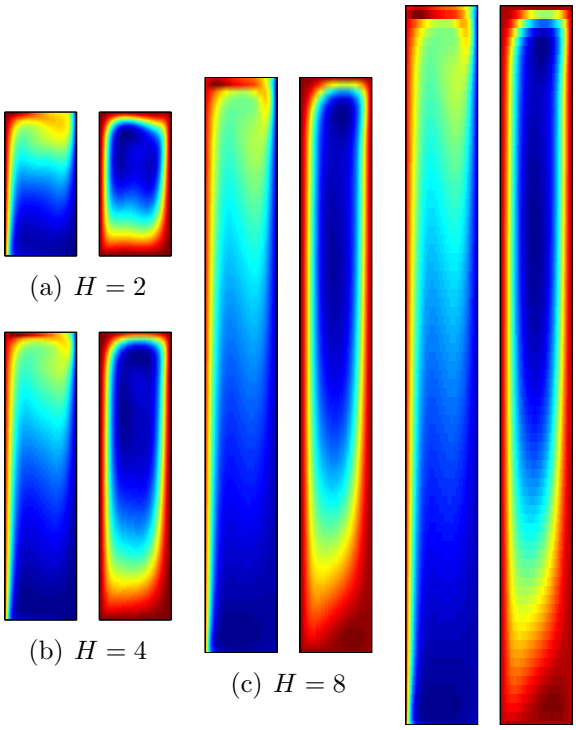

(a) $H = 2$

(b) $H = 4$

(c) $H = 8$

(d) $H = 10$

Figure 4.8: The effect of aspect ratio on the isotherms and streamlines for Ra $= 10^5$ and $\kappa = 0.5$ and $N = 1$, case No. 9 - 12

Figure. 4.8 shows a group of simulation results with Ra $= 10^5, \kappa = 0.5$ and $N = 1$. Comparing to Figure 4.5, the streamlines are more uniform and isotherms less distorted. This is because convection is weaker for smaller Rayleigh numbers.

4.2.2 Effect of Radius Ratio

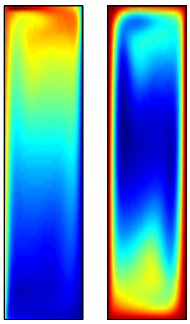

(a) $\kappa = 0.8$

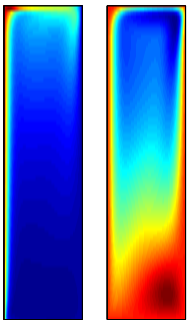

(c) $\kappa = 0.2$

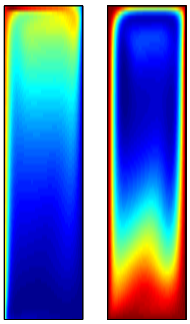

(b) $\kappa = 0.5$

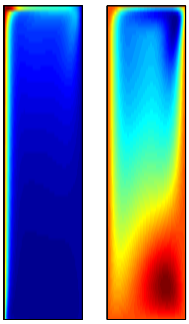

(d) $\kappa = 0.1$

Figure 4.9: The effect of radius ratio on the isotherms and streamlines for Ra $= 10^6, A = 4$ and $N = 1$, case No. 13-16

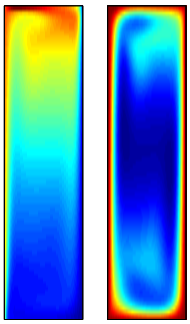

(a) $\kappa = 0.8$

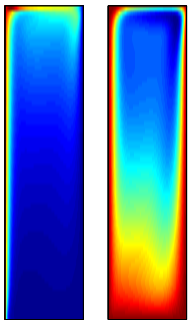

(c) $\kappa = 0.2$

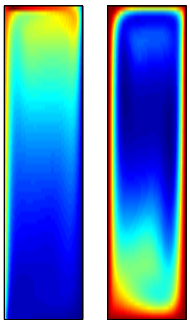

(b) $\kappa = 0.5$

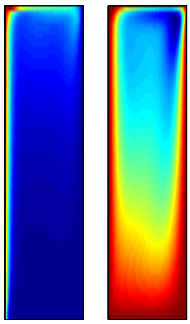

(d) $\kappa = 0.1$

Figure 4.10: The effect of radius ratio on the isotherms and streamlines for Ra $= 10^6, A = 4$ and $N = 10$, case No. 17-20

Figure. 4.9 and Figure. 4.10 show the effect of radius ratio on the temperature profile and flow structure with Ra $= 10^6, A = 4, N = 1$ and $N = 10$, respectively. In Figure.4.9 (a) when $\kappa = 0.8$, i.e. narrower annular space, the occurrence of a recirculation cell at each of the upper left and lower right corners of the streamline enclosure is seen. As the radius ratio decreases, these convection cells merge into one major cell. Moreover, for a larger aspect ratio $\kappa = 0.8$, the isotherms penetrate through the whole region while for small aspect ratio $\kappa = 0.1$ the isotherms penetrate only part of the region. This phenomenon can be explained by that as radius ratio increases, the gap of the annulus becomes smaller, therefore it is easier for thermal energy to transport.

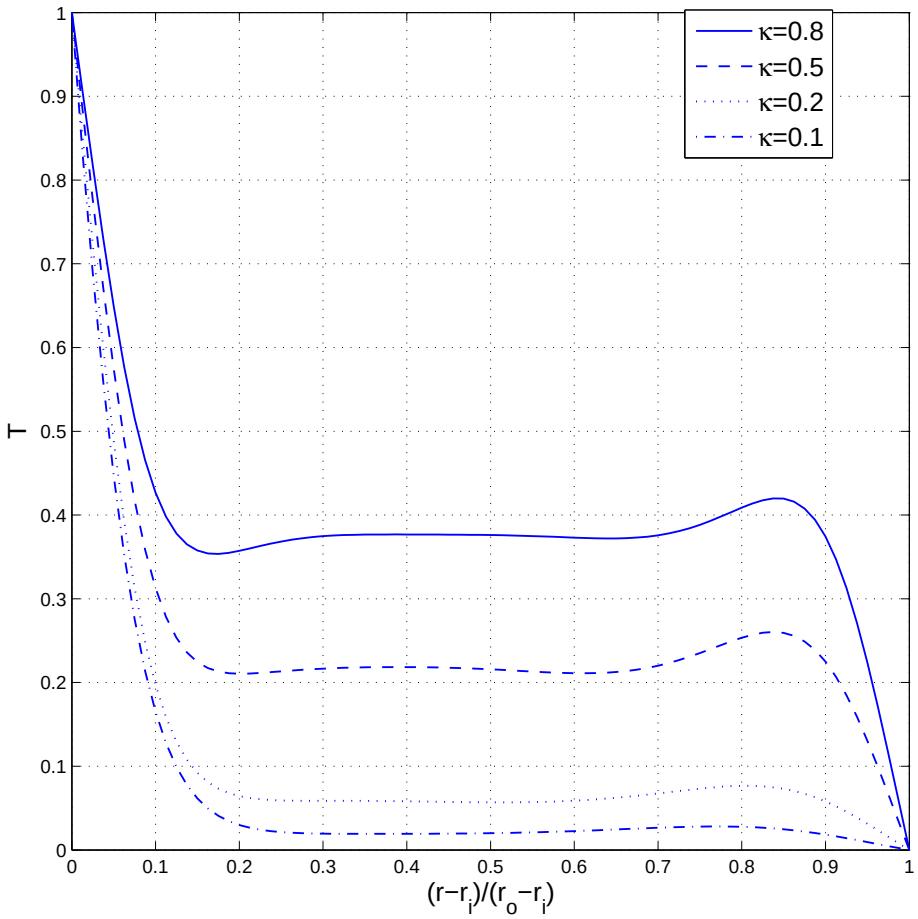

Figure 4.11: The effect of radius ratio on the temperature profile at $z = 0.5H$ for $\mathrm{Ra} = 10^6, H = 4$ and $N = 1$

Figure 4.11 depicts the effect of radius ratio on the temperature profile at the horizontal mid plane for $\mathrm{Ra} = 10^6, H = 4$, and $N = 1$. As the radius ratio increases, the temperature increases sharply, due to the curvature effect.

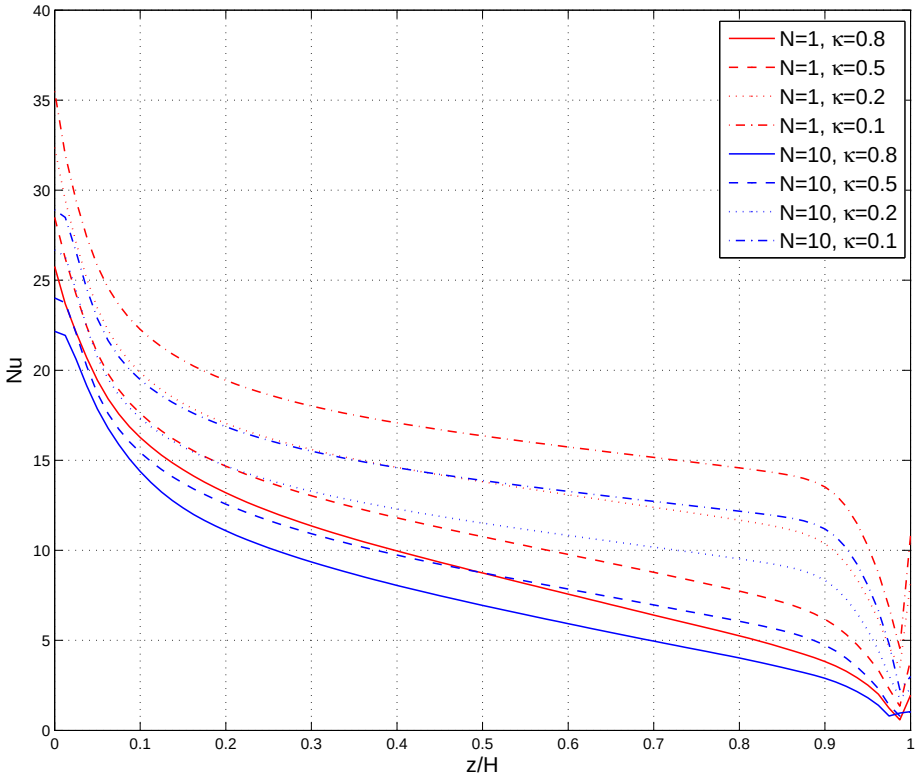

Figure 4.12: The effect of radius ratio on local Nusselt number along the inner annulus wall at $z = 0.5H$ for $\mathrm{Ra} = 10^6, H = 4$, for $N = 1$

Figure 4.12 illustrates the effect of radius ratio on local Nusselt number along inner cylinder wall with $\mathrm{Ra} = 10^6, H = 4$, $N = \infty$ and 1. Again we can see the contribution of radiation to the local heat transfer rate, as local Nusselt number along inner cylinder wall is higher when $N = 1$ than $N = \infty$. For a fixed N, the local Nusselt numbers increase as the radius ratio increases, which can be explained by the curvature effect too.

4.3 Effects of Dimensionless Time

The groups of simulations in this section are aimed to show the algorithm's capability and robustness in simulating the heat transfer within a very long vertical annulus, which is the usual configuration of wellbore annuli. The effect of dimensionless time on the flow structure and heat transfer characteristics is also demonstrated.

Figure 4.13 shows the simulation results of pure convection within a tall annulus with Ra $= 1.42E4, H = 20, \kappa = 0.8$. The transient isotherms and streamlines are captured with a dimensionless time increment of 0.05. From the streamlines, we can tell that multiple convection cells develops in the plane and rise upward along time. This phenomenon leads to the oscillations in the isotherms as well as in the local Nusselt number along inner cylinder wall.

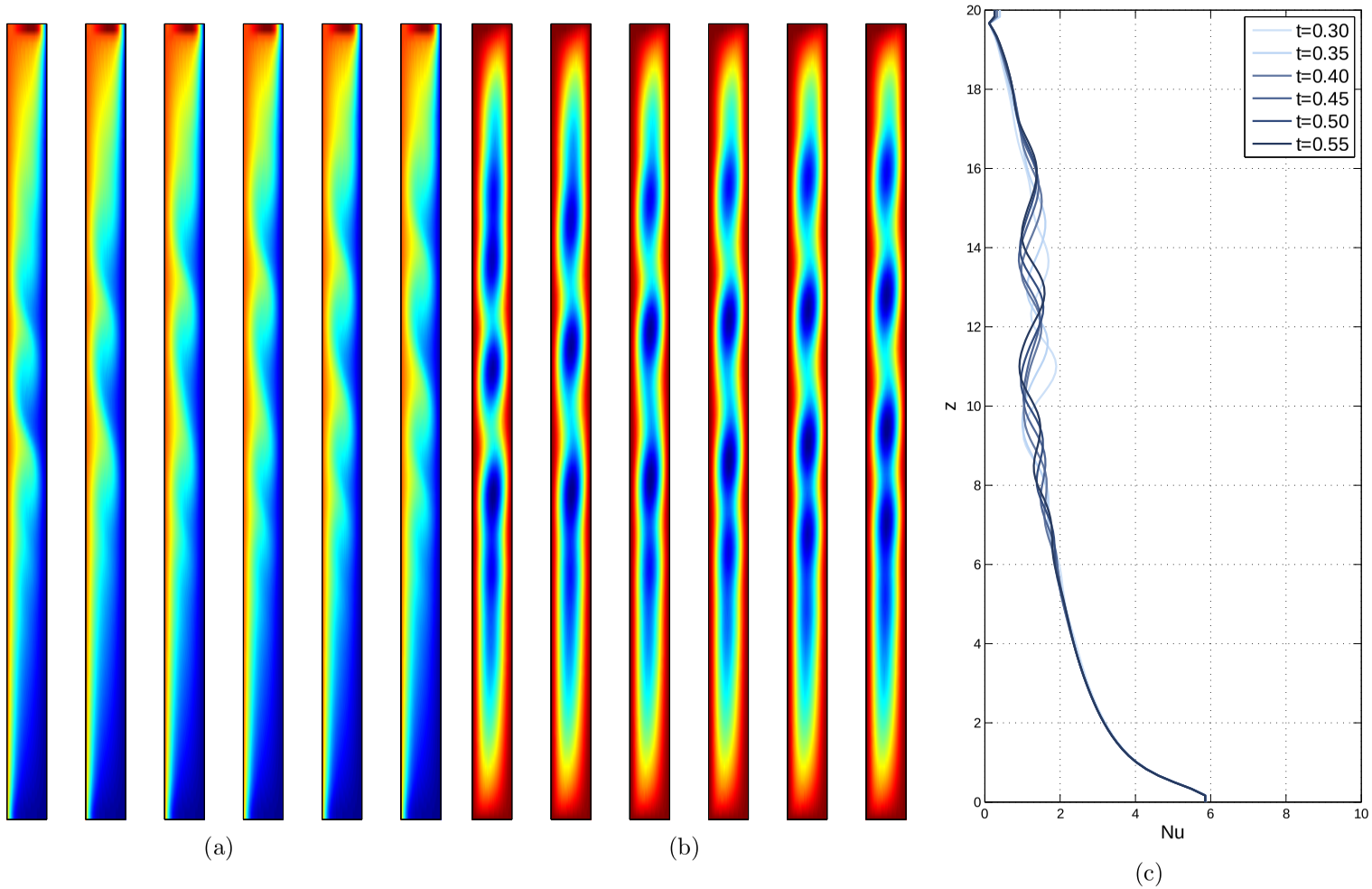

(a) (b) (c)

Figure 4.13: Isotherms (a), streamlines (b) and local Nusselt number along inner cylinder wall at dimensionless time of 0.30, 0.35, 0.40, 0.45, 0.50, 0.55 with Ra $= 1.42E4, H = 20, \kappa = 0.8$ and $N = \infty$

Figure 4.14 demonstrates a corresponding simulation with Ra $= 1.42E4, H = 20, \kappa = 0.8$ and $N = 1$. In the streamlines, multiple convection cells form at first and merge into one big cell as time passes by. The local Nusselt number along inner cylinder wall are larger compared with the pure convection case.

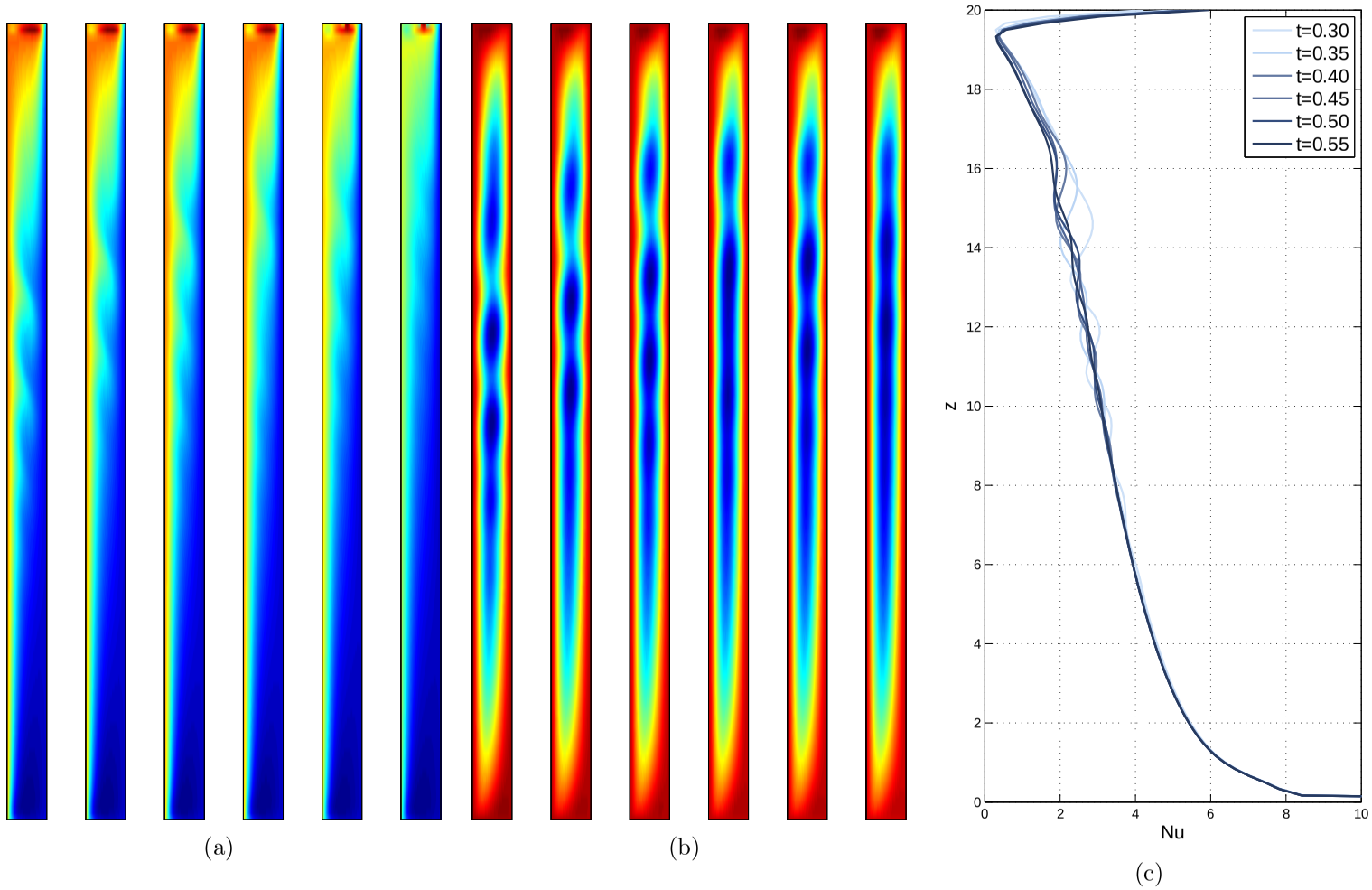

Figure 4.14: Isotherms (a), streamlines (b) and local Nusselt number along inner cylinder wall at dimensionless time of 0.30, 0.35, 0.40, 0.45, 0.50, 0.55 with Ra $= 1.42E4, H = 20, \kappa = 0.8$ and $N = 1$

Chapter 5

APPLICATION IN VACUUM INSULATED TUBING COMPLETED WELLBORE SIMULATION

In Chapter 4 the accuracy and applicability of the developed module of annulus heat transfer are demonstrated through series of validation tests and experimental tests. In this Chapter, the developed module is applied by coupling to a stand-alone thermal wellbore simulator developed by Xiong [69] for case studies of VIT completed wellbore heat transfer simulation.

5.1 Overview of the Standalone Thermal Wellbore Simulator

The Standalone Thermal Wellbore Simulator is recently developed by Xiong in 2015 [69]. It is a multi-phase, multi-component, transient, thermal and fully-implicit wellbore simulator. It has the capacity of modelling different complex wellbore configurations including horizontal wells and wells completed with dual tubing.

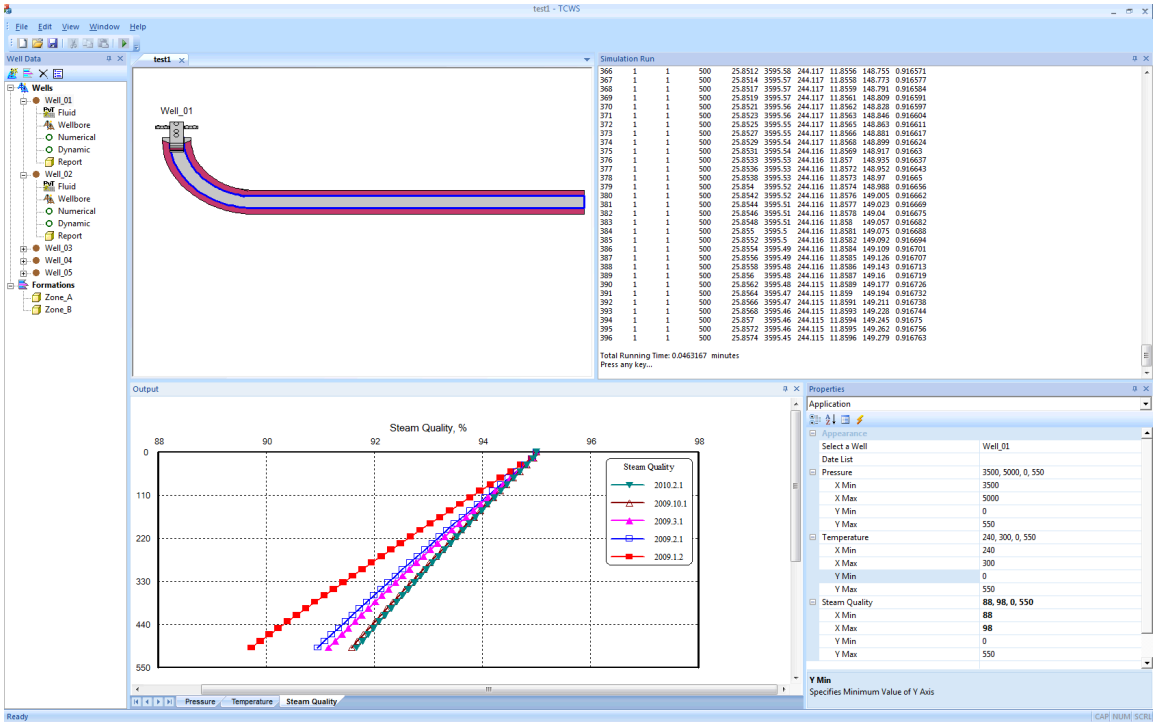

Figure 5.1: The Standalone Thermal Wellbore Simulator, Copyright ©2016 by Reservoir Simulation Group, University of Calgary

In the original simulator, a series of FLUENT simulations were run with different tubing temperature, casing temperature, tubing radius and casing radius to calculate the convective heat transfer within the annuli. FLUENT simulations were also run on annulus enclosed by dual-tubing completions. Correlations between Nusselt number and Rayleigh number were regressed based on simulation results, and embedded in the wellbore simulator to improve heat loss calculations. For more details on the Standalone Thermal Wellbore Simulator, the reader is referred to Xiong's thesis [68]. In this chapter, the developed annulus heat transfer module is coupled to the wellbore simulator to replace the original correlations.

5.2 Marlin Well A-6 Data

In 2002 a series of three papers [10] [18] [23] addressed the failure of Well A-2 on the Marlin tension leg platform (TLP) located in the Gulf of Mexico. By analyzing the physical evidence, the primary failure mechanism is identified to be the incremental annulus fluid expansion (AFE) pressure in the annuli [10]. Based on this failure analysis, a redesign process using VIT for the remaining Marlin wells was proposed [18]. Well A-6 is chosen for a full-scale test of VIT, with fiber-optic cable run on completion to continuously monitor the production-annulus temperature [23]. In this section, the Marlin Well A-6 data is used for the case study. Figure. 5.2 shows a schematic of Marlin A-6 Well. All parameters are originally in field units, in this study, they are converted to SI units. Terminology used are summarized in Table 5.1, parameters are listed in Table 5.2. Design parameters of vacuum insulated tubing are summarized in Table 5.3.

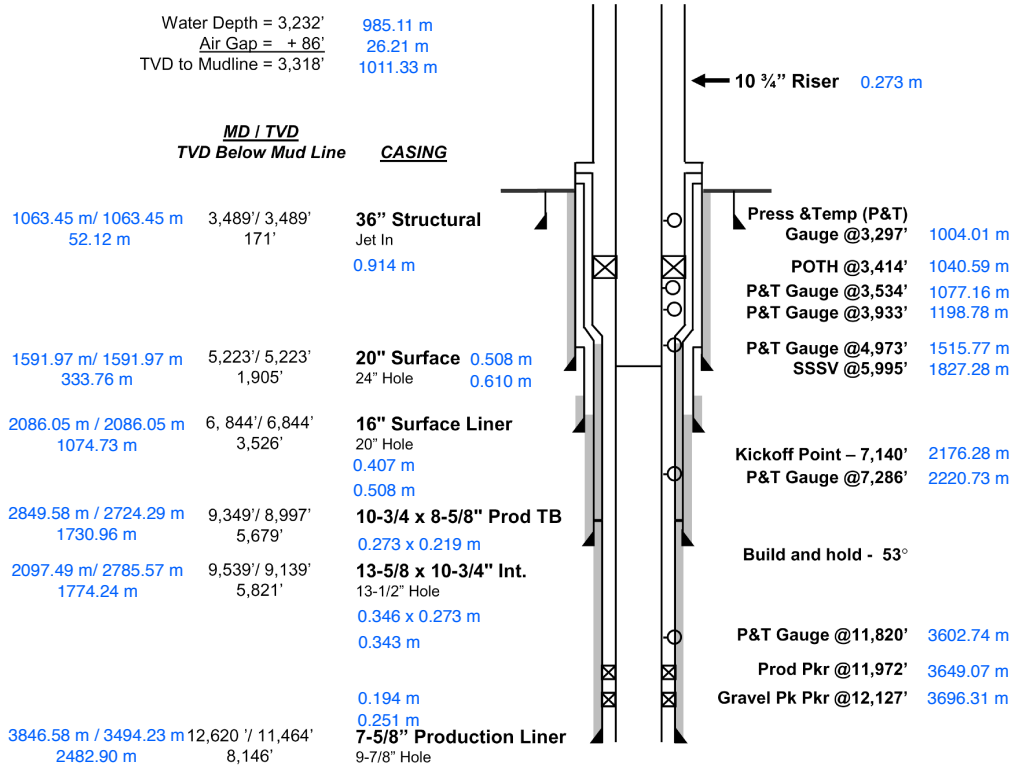

Figure 5.2: Schematic of Marlin Well A-6, subtracted from Gosch et al. 2002 [23]

Table 5.1: Terminology for Marlin A-6 Well

Item	**Explanation**
POTH	the submudline tubing-hanger packer is called a **p**ack**o**ff **t**ubing **h**anger
A- annulus	the production tubing/tieback (5 1/2- × 10 3/4- in.) annulus
B- annulus	the annulus outside production tieback
C- annulus	the annulus outside the intermediate casing

Table 5.2: Summary of Design Parameters for Marlin A-6 Well Input Variables in SI Units

Variable	**Value**
Thermal conductivity of formation	0.865 w/m-°C for 0 to 121.92 m below mudline, 1.5916 w/m-°C deeper
Thermal conductivity for chrome	24.22 w/m-°C deeper
A-annulus fluid	Nitrogen from TLP to POTH, brine from POTH to total depth (TD)
B- and C-annulus fluids	Fresh water at the hydrostatic pressure of the installation fluid
POTH position	24.384 m below mudline
Flow rate	An initial production scenario sufficient to produce a flowing hydrocarbon temperature of 82.22°C
Mudcake	0.02699 m on both the 0.508 − ×0.407− m surface casing and liner and the 0.346 − ×0.273− m intermediate casing

Table 5.3: Design parameters of the vacuum insulated tubing

size	7 1/16- × 5 1/2- in. (0.1178 × 0.1397 m) above POTH, 5 1/2- × 4 1/2- in. (0.1397 × 0.1016 m) below POTH
VIT unit length	approximately 40 ft. (12.192 m)
coupling length	approximately 3 ft. (0.914 m)
Thermal conductivity of VIT pipe	0.0346 w/m-°C
Thermal conductivity of VIT couping	45.326 w/m-°C

A fiber-optic cable is run along the production annulus to continuously collect the production casing temperature data. Typical output temperature data is shown in Figure 5.3. The temperature profile demonstrates severe zig-zag pattern. By expansion of a segment of the profile, shown in Figure 5.4, we can clearly detect the temperature spikes in the casing temperature profile. The spikes occur regularly, roughly every 40 ft., which is in consistence with the locations of VIT couplings along the wellbore.

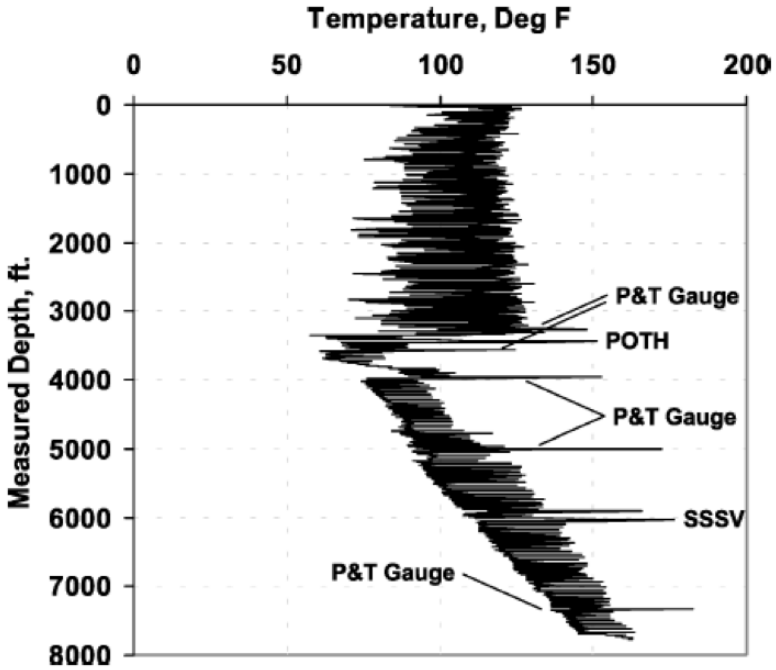

Figure 5.3: Typical output of the Marlin Well fiber-optic installation, subtracted from Gosch et al. 2002 [23]

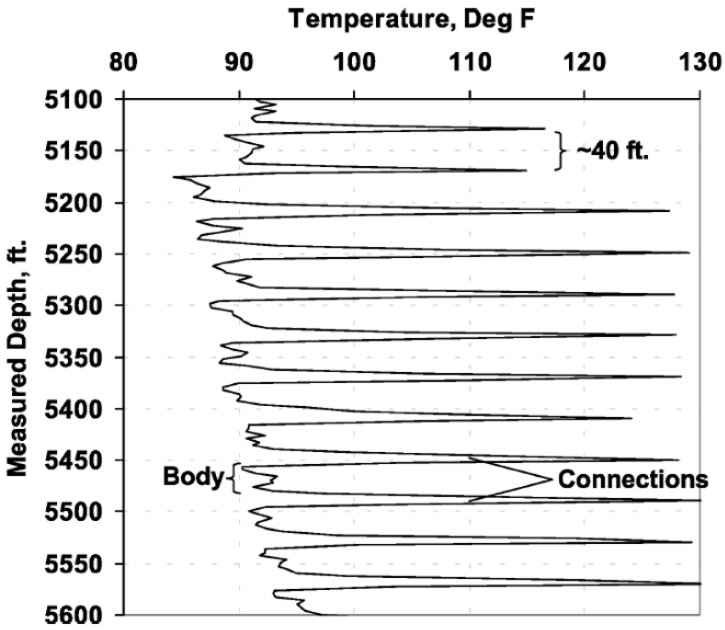

Figure 5.4: Typical output of the Marlin Well fiber-optic installation, subtracted from Gosch et al. 2002 [23]

5.3 Annulus Fluid Thermal Properties

Fluid thermal properties are correlated to temperature through regression, for four types of annulus fluid: air, nitrogen, water and brine (11 lb/gal CaCl2 brine). Symbols and units are listed in Table. 5.4. Due to space limitations the original datasets used for regression are listed in Appendix B. The following correlations are embedded in the program such that thermal properties can be calculated automatically when the fluid type and reference temperatures are specified.

Table 5.4: Annulus Fluid Thermal Properties and Units

Symbol	**Definition**	**Unit**
T	reference temperature	K
ρ_0	density	kg/m^3
c_p	specific heat capacity	kJ/kg·K
k	thermal conductivity	W/m·K
μ	dynamic viscosity	Pa.s
β	thermal expansion coefficient	1E-3 1/K

5.3.1 Air Thermal Properties

The following correlations for air thermal properties are valid in a temperature range T from 273.15 K to 673.15 K:

$$\rho_0 = -9.03741E{-}09T^3{+}1.68507E{-}05T^2{-}1.14308E{-}02T{+}3.33646, \quad R^2 = 0.999982$$

$$c_p = -6.84638E{-}10T^3{+}1.26091E{-}06T^2{-}5.50107E{-}04T{+}1.07539, \quad R^2 = 0.996294$$

$$k = 6.900488E-05T + 5.660888E-03, \quad R^2 = 0.9990451$$

$$\mu = 3.890163E-08T + 7.164925E-06, \quad R^2 = 0.9953380$$

$$\beta = 1.198E-05T^2 - 0.01646T + 7.197, \quad R^2 = 0.9963272$$

5.3.2 Nitrogen Thermal Properties

The following correlations for nitrogen thermal properties are valid in a temperature range T from 273.15 K to 673.15 K:

$$\rho_0 = 4E-06T^2 - 0.0056T + 2.4407, \quad R^2 = 0.9962$$

$$c_p = 3E-07T^2 - 0.0002T + 1.0683, \quad R^2 = 0.999$$

$$k = 0.0594T + 8.4392, \quad R^2 = 0.9992$$

$$\mu = 0.0382T + 6.7241, \quad R^2 = 0.9967$$

$$\beta = 1E-05T^2 - 0.0163T + 7.1609, \quad R^2 = 0.9963$$

5.3.3 Water Thermal Properties

The following correlations for water thermal properties are valid in a temperature range T from 273.15 K to 373.15 K:

$$\rho_0 = -0.0035T^2 + 1.1231T + 911.68, \quad R^2 = 0.9997$$

$$c_p = -9E-08T^3 + 7E-05xT^{-}0.0188T + 5.7227, \quad R^2 = 0.9909$$

$$k = -0.0099T^2 + 5.599T - 114.4, \quad R^2 = 0.9999$$

$$\mu = -2E-06T^3 + 0.0016T^2 - 0.4142T + 35.425, \quad R^2 = 0.9994$$

$$\beta = -2E-06T^3 + 0.0016T^2 - 0.399T + 34.269, \quad R^2 = 0.9995$$

5.3.4 Brine Thermal Properties

The brine selected is 11 lb/gal CaCl2 brine. The following correlations are valid in a temperature range T from 273.15 K to 373.15 K:

$$\rho_0 = -0.3322T + 1409.3, \quad R^2 = 0.9988$$

$$c_p = 0.0014T + 2.2981, \quad R^2 = 0.9993$$

$$k = 0.0603T + 25.832, \quad R^2 = 0.9995$$

$$\mu = -2E - 05T^3 + 0.017T^2 - 6.0602T + 724.04, \quad R^2 = 0.9991$$

$$\beta = 0.46$$

5.4 Numerical Settings

Numerical parameters are designed to be read from the input file and thus can be specified outside the program. The parameters used for the case study are listed in Table 5.5.

Table 5.5: Numerical controls for annulus heat transfer simulation in the present case study

Parameter	**Value**
Number of grids along radial direction	21
Number of grids along axial direction	21
Dimensionless time step	0.001
Convergence tolerance for inner iterations	1.0E-7
Maximum number of inner iteration	50
Convergence tolerance for Newton-Raphson iteration	1.0E-6
Maximum number of Newton-Raphson iteration	50
Convergence tolerance for the linear solver	1.0E-8
Maximum number of the linear solver iteration	150

5.5 Simulation Results and Analysis

Simulations were run with Marlin Well A-6 data presented above. The annulus fluid properties are calculated using the correlations provided. Since the primary objective of this case study is to examine the heat transfer characteristics of vacuum insulated tubing, only a segment of the whole wellbore was simulated. The fluid temperature, fluid pressure and casing temperature profiles were obtained, for time 0.01 day, 2 days, 1 month, 2 months and 3 months, shown in Figure 5.5, Figure 5.6 and Figure 5.7 respectively.

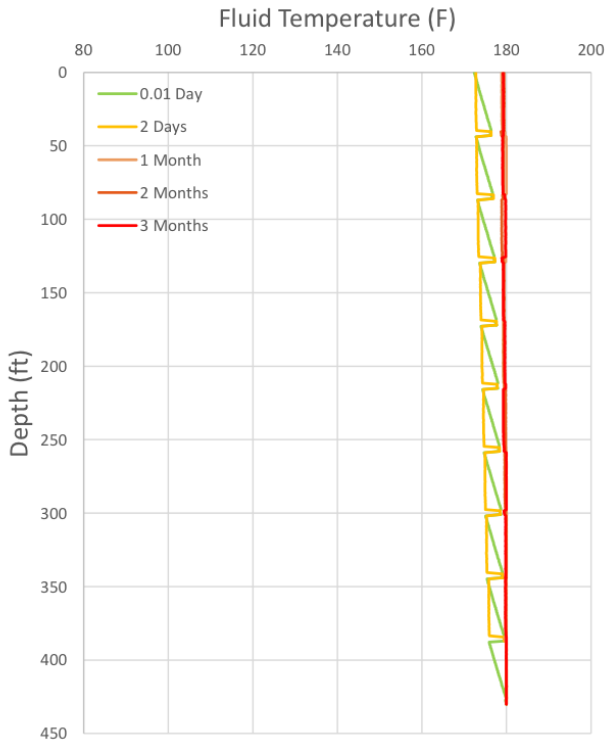

Figure 5.5: Simulation results of tubing fluid temperature at 0.01 day, 2 days, 1 month, 2 months and 3 months

As shown in Figure 5.5, the tubing fluid temperature profile exhibits a zig-zag pattern consistent with the location of vacuum insulated tubing couplings at 0.01 day and 2 days as the production is initialized. After the production of 1 month the tubing fluid temperature reaches a stable state. The fluid temperature is almost

constant within the depth of our investigation.

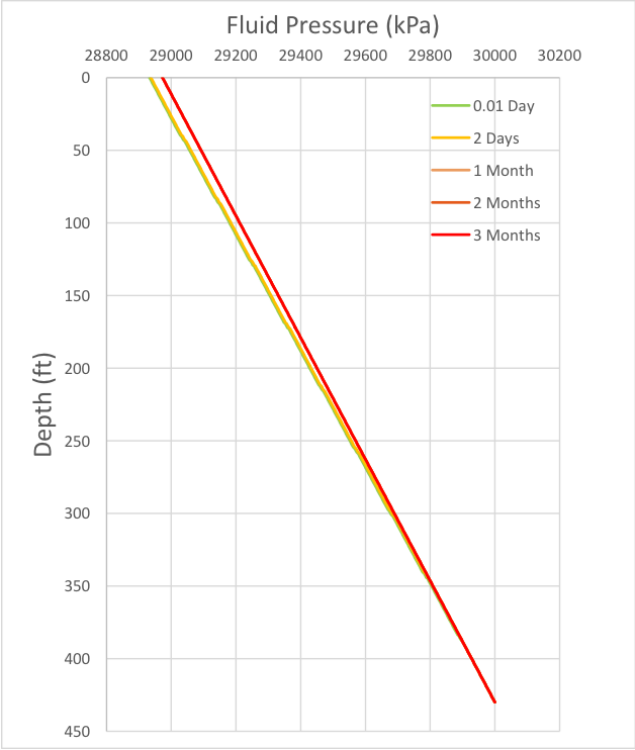

Figure 5.6: Simulation results of tubing fluid pressure at 0.01 day, 2 days, 1 month, 2 months and 3 months

Figure 5.6 shows the tubing fluid pressure profile, at the time of 0.01 day, 2 days, 1 month, 2 months and 3 months. Tubing fluid pressure increases as the depth increases, and is stable along the production time.

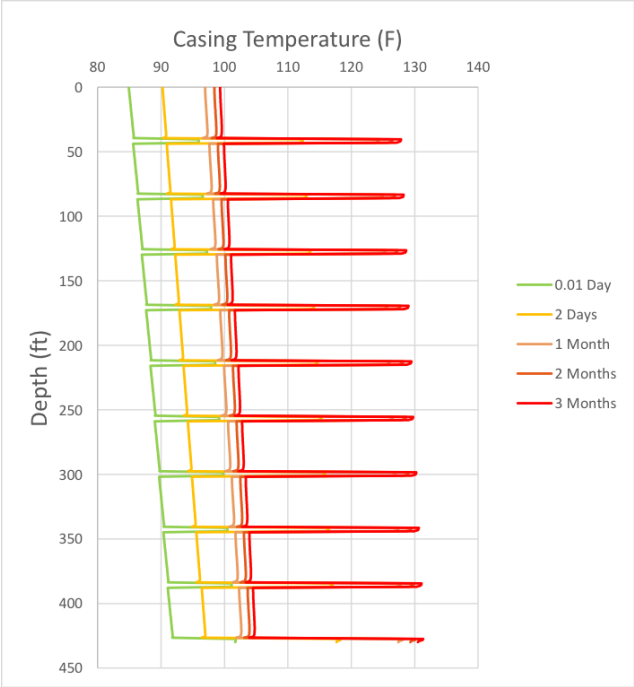

Figure 5.7: Simulation results of casing temperature profiles at 0.01 day, 2 days, 1 month, 2 months and 3 months

Casing temperature profiles are also obtained from the simulation study, shown in Figure 5.7. By comparing with the field data of a segment of measured casing temperature profile displayed in Figure 5.4, it is evident that the research simulation precisely captures the temperature spikes, indicating that the new simulator is accurate and reliable. The temperature spikes can be explained by the higher heat transfer rate at the couplings, which is clearly demonstrated by the overall heat transfer coefficient. The overall heat transfer coefficient of both VIT pipe and VIT coupling are listed in Table 5.6.

Table 5.6: Overall heat transfer coefficient U_{to} of VIT pipe and VIT coupling

Variable	**Value**
Overall heat transfer coefficient U_{to} of VIT pipe	1.81554 W/m^2°C
Overall heat transfer coefficient U_{to} of VIT coupling	5.64513 W/m^2°C

The multicellular convection in VIT annulus induced by the hot couplings plays a critical role and significantly decrease the VIT overall insulation efficiency. It must

be well analyzed to determine heat loss through VIT and prevent tubular failure due to much higher thermal stress in the tubular and the annulus pressure buildup (APB) than expected.

Chapter 6

CONCLUSIONS AND FUTURE WORKS

This study addressed the conjugate natural convection and radiation within thermal wellbore annuli using a rigorous mathematical model and numerical simulation, which to the author's knowledge has not been done before. The major contributions of this thesis are reported below followed by recommendations for future work.

6.1 Conclusions

1. A novel 2D transient mathematical model of the conjugate natural convection and radiation within thermal wellbore annuli is proposed. A vorticity- steam function based approach is used to form the governing equations. This method avoids the calculation of pressure terms and results in relatively succinct solution algorithms.

2. An efficient and robust numerical scheme involving second-order upstream method and Newton-Raphson iteration is developed and validated. The scheme demonstrates its merit when convection and radiation are strong, as well as when the aspect ratio is very high.

3. A flexible module of annulus heat transfer simulation is developed in C++, and fully coupled to a standalone thermal wellbore simulator. The significance of the developed module is shown by a case study of vacuum insulated tubing (VIT) heat transfer simulation. The new

simulator precisely captures the temperature spikes along casing temperature profile, and accurately calculates heat loss within the wellbore.

6.2 Recommendations for Future Work

There is still lots of work required to improve the features of the developed program and the further development of a thermal wellbore simulation. The work to be done is summarized as follows:

1. Analyze the casing thermal stress and annulus pressure build up based on the present simulation results. This analysis is critical to thermal wellbore integrity and constructive to well design.

2. Conduct a full-scale simulation of hot fluid injection through VIT versus bare tubing to justify VIT's insulation efficiency in both short term and long term.

3. Simulate the conjugate natural convection and radiation within the annulus space enclosed by a dual-string completion. Since the annulus space of this kind is irregular, a 3D model is required. Unstructured mesh (can be generated by Delauney triangulation) is needed for discretization. A new discretization scheme and solution algorithms that adapt to the unstructured mesh are also needed.

4. Continue to study the types of annulus fluid thermal properties, especially the radiative properties. For a material, the radiative *absorption coefficient* depends on the frequency of the absorbed wave and the temperature of the material. In the present radiation model, an average number of absorption coefficient is used as the gray fluid assumption

indicates. Therefore a delicate determination of average value is needed for any annulus fluid.

5. Simulate the evaporation and condensation process for a wet annulus. The literature has shown that for a wet annulus, evaporation at the hot joint and condensation at relatively cold tubing wall will lead to more heat loss.

Bibliography

[1] D. Aeschliman, R. Meldau, N. Noble, et al. Thermal efficiency of a steam injection test well with insulated tubing. In *SPE California Regional Meeting*. Society of Petroleum Engineers, 1983.

[2] J. Azzola, P. Pattillo, J. Richey, S. Segreto, et al. The heat transfer characteristics of vacuum insulated tubing. In *SPE Annual Technical Conference and Exhibition*. Society of Petroleum Engineers, 2004.

[3] M. Bahonar. Transient non-isothermal wellbore fluid flow and heat transfer modeling.

[4] M. Bahonar, J. Azaiez, Z. Chen, et al. A semi-unsteady-state wellbore steam/water flow model for prediction of sandface conditions in steam injection wells. *Journal of Canadian Petroleum Technology*, 49(09):13–21, 2010.

[5] M. Bahonar, J. Azaiez, Z. Chen, et al. Transient nonisothermal fully coupled wellbore/reservoir model for gas-well testing, part 1: Modelling. *Journal of Canadian Petroleum Technology*, 50(9-10):37–50, 2011.

[6] M. Bahonar, J. Azaiez, Z. Chen, et al. Transient nonisothermal fully coupled wellbore/reservoir model for gas-well testing, part 2: Applications. *Journal of Canadian Petroleum Technology*, 50(9-10):51–70, 2011.

[7] M. Bahonar, J. Azaiez, Z. Chen, et al. Two issues in wellbore heat flow modelling along with the prediction of casing temperature in the steam injection wells. *Journal of Canadian Petroleum Technology*, 50(01):43–63, 2011.

[8] R. Barrett, M. W. Berry, T. F. Chan, J. Demmel, J. Donato, J. Dongarra, V. Eijkhout, R. Pozo, C. Romine, and H. Van der Vorst. *Templates for the*

solution of linear systems: building blocks for iterative methods, volume 43. Siam, 1994.

[9] J. Bellarby. *Well completion design*, volume 56. Elsevier, 2009.

[10] D. Bradford, D. Gibson, S. Gosch, P. Pattillo, J. Sharp, C. Taylor, et al. Marlin failure analysis and redesign; part 1, description of failure. In *IADC/SPE Drilling Conference*. Society of Petroleum Engineers, 2002.

[11] L. Caretto, A. Gosman, S. Patankar, and D. Spalding. Two calculation procedures for steady, three-dimensional flows with recirculation. In *Proceedings of the third international conference on numerical methods in fluid mechanics*, pages 60–68. Springer, 1973.

[12] Z. Chen. *Reservoir simulation: mathematical techniques in oil recovery*, volume 77. Siam, 2007.

[13] Z. Chen, G. Huan, and Y. Ma. *Computational methods for multiphase flows in porous media*, volume 2. Siam, 2006.

[14] R. Courant, E. Isaacson, and M. Rees. On the solution of nonlinear hyperbolic differential equations by finite differences. *Communications on Pure and Applied Mathematics*, 5(3):243–255, 1952.

[15] G. de Vahl Davis. Natural convection of air in a square cavity: a bench mark numerical solution. *International Journal for numerical methods in fluids*, 3(3):249–264, 1983.

[16] G. de Vahl Davis and R. Thomas. Natural convection between concentric vertical cylinders. *Physics of Fluids (1958-1988)*, 12(12):II–198, 1969.

[17] Dynalene, Inc. Calcium chloride series brines.

[18] R. Ellis, D. Fritchie Jr, D. Gibson, S. Gosch, P. Pattillo, et al. Marlin failure analysis and redesign; part 2, redesign. In *IADC/SPE Drilling Conference*. Society of Petroleum Engineers, 2002.

[19] S. M. Farouq Ali. *Practical Heavy Oil Recovery*. 2014.

[20] S. M. Farouq Ali et al. A comprehensive wellbore stream/water flow model for steam injection and geothermal applications. *Society of Petroleum Engineers Journal*, 21(05):527–534, 1981.

[21] S. M. Farouq Ali, R. Meldau, et al. Current steamflood technology. *Journal of Petroleum Technology*, 31(10):1–332, 1979.

[22] J. P. Fontanilla, K. Aziz, et al. Prediction of bottom-hole conditions for wet steam injection wells. *Journal of Canadian Petroleum Technology*, 21(02), 1982.

[23] S. Gosch, D. Horne, P. Pattillo, J. Sharp, P. Shah, et al. Marlin failure analysis and redesign; part 3, vit completion with real-time monitoring. In *IADC/SPE Drilling Conference*. Society of Petroleum Engineers, 2002.

[24] D. D. Gray and A. Giorgini. The validity of the boussinesq approximation for liquids and gases. *International Journal of Heat and Mass Transfer*, 19(5):545–551, 1976.

[25] A. Hasan, C. Kabir, et al. Aspects of wellbore heat transfer during two-phase flow (includes associated papers 30226 and 30970). *SPE Production & Facilities*, 9(03):211–216, 1994.

[26] A. R. Hasan, C. S. Kabir, D. Lin, et al. Analytic wellbore temperature model for transient gas-well testing. In *SPE Annual Technical Conference and Exhibition*. Society of Petroleum Engineers, 2003.

[27] A. R. Hasan, C. S. Kabir, X. Wang, et al. A robust steady-state model for flowing-fluid temperature in complex wells. *SPE Production & Operations*, 24(02):269–276, 2009.

[28] C. Ho and Y. Lin. Natural convection of cold water in a vertical annulus with constant heat flux on the inner wall. *Journal of heat transfer*, 112(1):117–123, 1990.

[29] J. A. Holmes et al. Modeling advanced wells in reservoir simulation. *Journal of petroleum technology*, 53(11):54–66, 2001.

[30] H. Huang and B. R. Seymour. The no-slip boundary condition in finite difference approximations. *International journal for numerical methods in fluids*, 22(8):713–729, 1996.

[31] H. H. Huygen, J. Huitt, et al. Wellbore heat losses and casing temperatures during steam injection. In *Drilling and Production Practice*. American Petroleum Institute, 1966.

[32] C. S. Kabir, A. R. Hasan, et al. Simplified wellbore flow modeling in gas-condensate systems. In *SPE Annual Technical Conference and Exhibition*. Society of Petroleum Engineers, 2004.

[33] Y. Kang, R. Samuel, A. Gonzales, Z. Liu, et al. Heat transfer modeling of wellbore with vacuum-insulated-tubing (vit). In *SPE Thermal Well Integrity and Design Symposium*. Society of Petroleum Engineers, 2015.

[34] T. Kuehn and R. Goldstein. An experimental and theoretical study of natural convection in the annulus between horizontal concentric cylinders. *Journal of Fluid mechanics*, 74(04):695–719, 1976.

[35] T. Kuehn and R. Goldstein. An experimental study of natural convection heat transfer in concentric and eccentric horizontal cylindrical annuli. *Journal of Heat Transfer*, 100(4):635–640, 1978.

[36] D.-C. Kuo, J. Morales, and K. Ball. Combined natural convection and volumetric radiation in a horizontal annulus: spectral and finite volume predictions. *Journal of heat transfer*, 121(3):610–615, 1999.

[37] P. Le Quéré. Accurate solutions to the square thermally driven cavity at high rayleigh number. *Computers & Fluids*, 20(1):29–41, 1991.

[38] P. Le Quéré and T. A. De Roquefortt. Computation of natural convection in two-dimensional cavities with chebyshev polynomials. *Journal of Computational Physics*, 57(2):210–228, 1985.

[39] Y. Lee, S. Korpela, and R. Horne. Structure of multi-cellular natural convection in a tall vertical annulus. In *Proc. 7th International Heat Transfer Conference, U. Grigul et al., eds., Hemisphere, Washington, DC*, volume 2, pages 221–226, 1982.

[40] Y. Lee and S. A. Korpela. Multicellular natural convection in a vertical slot. *Journal of Fluid Mechanics*, 126:91–121, 1983.

[41] B. Leonard. A survey of finite differences with upwinding for numerical modelling of the incompressible convective diffusion equation. *Computational Techniques in Transient and Turbulent Flow*, 2:1–35, 1981.

[42] B. P. Leonard. A stable and accurate convective modelling procedure based on quadratic upstream interpolation. *Computer methods in applied mechanics and engineering*, 19(1):59–98, 1979.

[43] B. P. Leonard and J. E. Drummond. Why you should not use hybrid,power-lawor related exponential schemes for convective modellingthere are much better alternatives. *International Journal for Numerical Methods in Fluids*, 20(6):421–442, 1995.

[44] S. Livescu, L. Durlofsky, and K. Aziz. A semianalytical thermal multiphase wellbore-flow model for use in reservoir simulation. *SPE journal*, 15(03):794–804, 2010.

[45] M. F. Modest. *Radiative heat transfer*. Academic press, 2013.

[46] M. Napolitano, G. Pascazio, and L. Quartapelle. A review of vorticity conditions in the numerical solution of the ζ–ψ equations. *Computers & Fluids*, 28(2):139–185, 1999.

[47] National Institute of Standards and Technology. Iml++ (iterative methods library) v.1.2a.

[48] National Institute of Standards and Technology. Sparselib++.

[49] E. Pacheco, S. Ali, et al. Wellbore heat losses and pressure drop in steam injection. *Journal of Petroleum Technology*, 24(02):139–144, 1972.

[50] S. Patankar. *Numerical heat transfer and fluid flow*. CRC press, 1980.

[51] S. V. Patankar. A calculation procedure for two-dimensional elliptic situations. *Numerical Heat Transfer*, 4(4):409–425, 1981.

[52] P. Pattillo, J. Bellarby, G. Ross, S. Gosch, G. McLaren, et al. Thermal and mechanical considerations for design of insulated tubing. *SPE Drilling & Completion*, 19(03):181–188, 2004.

[53] Peace Software. Nitrogen thermodynamic properties calculator.

[54] H. Ramey Jr et al. Wellbore heat transmission. *Journal of Petroleum Technology*, 14(04):427–435, 1962.

[55] SIAM. The history of numerical analysis and scientific computing.

[56] W. F. Spotz. Accuracy and performance of numerical wall boundary conditions for steady, 2d, incompressible stream-function vorticity. *International Journal for Numerical Methods in Fluids*, 28(4):737–757, 1998.

[57] W. Q. Tao. *Numerical heat transfer*. Xian Jiaotong University Press, Xian, 2001.

[58] W. Q. Tao. Recent advancement in numerical heat transfer, 2005.

[59] S. Thakur and W. Shyy. Some implementational issues of convection schemes for finite-volume formulations. *Numerical Heat Transfer, Part B Fundamentals*, 24(1):31–55, 1993.

[60] The Engineering Toolbox. Air properties.

[61] The Engineering Toolbox. Water - thermal properties.

[62] R. Thomas and G. de Vahl Davis. Natural convection in annular and rectangular cavities. a numerical study. Report, Univ. of New South Wales, Kensington, Australia, 1970. CANNOT FIND.

[63] D. Turney. Properties of water in the range 0 - 100 °c.

[64] L.-C. Weng and H.-S. Chu. Combined natural convection and radiation in a vertical annulus. *Heat and mass transfer*, 31(6):371–379, 1996.

[65] G. P. Willhite et al. Over-all heat transfer coefficients in steam and hot water injection wells. *Journal of Petroleum Technology*, 19(05):607–615, 1967.

[66] J.-Z. Wu, X.-H. Wu, H.-Y. Ma, and J.-M. Wu. Dynamic vorticity condition: Theoretical analysis and numerical implementation. *International journal for numerical methods in fluids*, 19(10):905–938, 1994.

[67] Y.-S. Wu, K. Pruess, et al. An analytical solution for wellbore heat transmission in layered formations (includes associated papers 23410 and 23411). *SPE Reservoir Engineering*, 5(04):531–538, 1990.

[68] W. Xiong. Development of a standalone thermal wellbore simulator, 2014.

[69] W. Xiong, M. Bahonar, Z. Chen, et al. Development of a thermal wellbore simulator with focus on improving heat loss calculations for sagd steam injection. In *SPE Canada Heavy Oil Technical Conference*. Society of Petroleum Engineers, 2015.

Appendix A

Convection Term Modifications for Border Control Volumes

Discretization using second-order upwind scheme leads to a nine-point stencil for 2D problems. As illustrated in Figure A.1, a modification on the discretization is needed for control volumes adjacent to the boundaries [59].Taking an arbitrary variable ϕ for example, the convection term writes

$$\left(u\frac{\partial\phi}{\partial r}+w\frac{\partial\phi}{\partial z}\right).$$

In the following sections, discussion will focus on the discretization of the convection term for border control volumes in different scenarios.

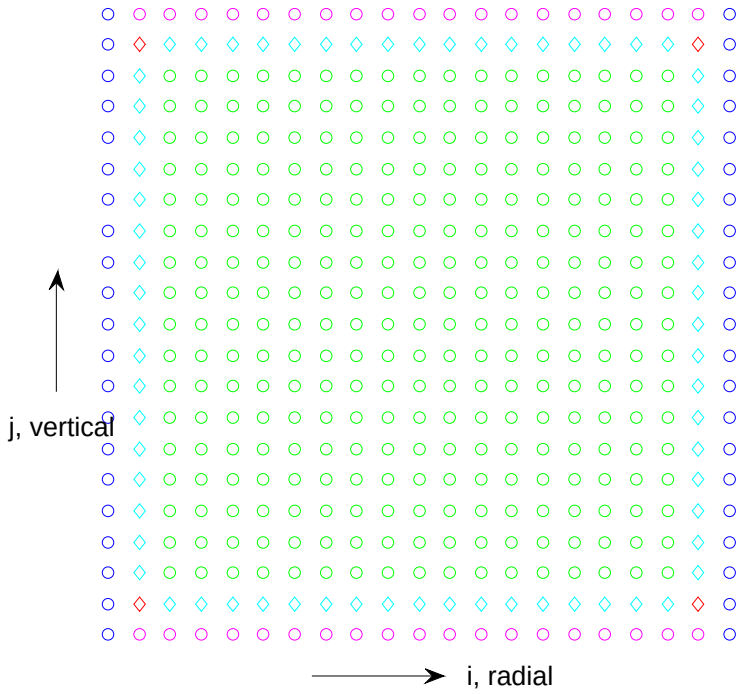

Figure A.1: A sketch of mesh used for discretization

A.1 Left Border Control Volume

Consider a typical border point P adjacent to the left boundary, shown in Fig.A.2. In the axial direction, each of ϕ_n and ϕ_s has two upwind neighbours in each direction. As long as the control volume is not on the corner, the original second-order upwind scheme can be used for its discretization along axial direction. In the radial direction, ϕ_e can be estimated using second-order upwind scheme, as two upwind neighbours exists in each direction. However P only has one neighbour on its left (namely, W). If the flux u_w is from the left boundary, i.e. $u_w > 0$ only schemes involves one neighbour is valid, such as the first order upwind or central difference. In the present study, the central difference is used for this scenario. If the flux u_w comes toward the west face from the interior of the domain, i.e. $u_w < 0$, as two neighbours exist on the right

hand side and second-order upwind scheme can be deployed.

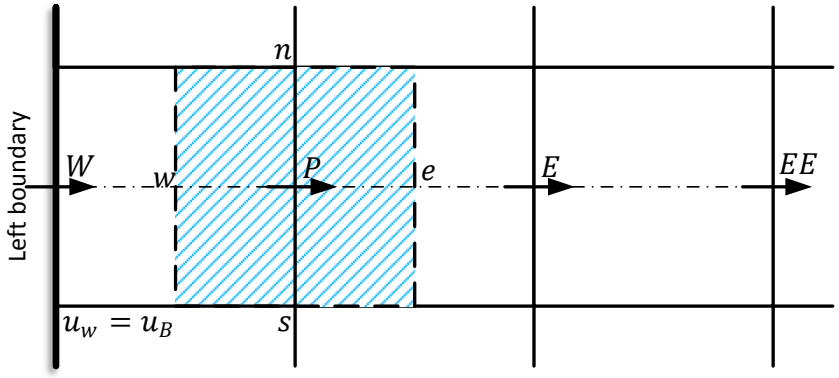

Figure A.2: Schematic of border (near boundary) control volume: a typical left border u control volume

To sum up, the discretization for $w\frac{\partial\phi}{\partial z}$ remains unchanged, the discretization for $u\frac{\partial\phi}{\partial r}$ writes,

$$\mathscr{D}\left(u\frac{\partial\phi}{\partial r}\right) = \frac{u_e\phi_e}{\Delta r} - \frac{u_w\phi_w}{\Delta r}$$

where on the east face, the second order upwind scheme

$$\frac{u_e\phi_e}{\Delta r} = (1.5\phi_P - 0.5\phi_W)[\![u_e, 0]\!]/\Delta r - (1.5\phi_E - 0.5\phi_{EE})[\![-u_e, 0]\!]/\Delta r$$

remains unchanged.

On the west face,

$$-\frac{u_w\phi_w}{\Delta r} = -0.5(\phi_W + \phi_P)[\![u_w, 0]\!]/\Delta r + (1.5\phi_P - 0.5\phi_E)[\![-u_w, 0]\!]/\Delta r$$

i.e second-order upwind scheme is applied when $u_w < 0$, central difference is applied when $u_w > 0$.

The convection term coefficients $\boldsymbol{F}^{\text{left}}$ for control volumes adjacent to the left

boundary is written as

$$F_{SS} = 0.5[\![w_s, 0]\!]/\Delta z \tag{A.1- 1a}$$

$$F_S = -1.5[\![w_s, 0]\!]/\Delta z - 0.5[\![w_n, 0]\!]/\Delta z \tag{A.1- 1b}$$

$$F^*_{WW} = 0 \tag{A.1- 1c}$$

$$F^*_W = -0.5[\![u_e, 0]\!]/\Delta r - 0.5[\![u_w, 0]\!]/\Delta r \tag{A.1- 1d}$$

$$\begin{aligned} F^*_P = {} & 1.5[\![u_e, 0]\!]/\Delta r + 1.5[\![-u_w, 0]\!]/\Delta r + 1.5[\![w_s, 0]\!]/\Delta z \\ & + 1.5[\![-w_n, 0]\!]/\Delta z - 0.5[\![u_w, 0]\!]/\Delta r \end{aligned} \tag{A.1- 1e}$$

$$F_E = -1.5[\![-u_e, 0]\!]/\Delta r - 0.5[\![-u_w, 0]\!]/\Delta r \tag{A.1- 1f}$$

$$F_{EE} = 0.5[\![-u_e, 0]\!]/\Delta r \tag{A.1- 1g}$$

$$F_N = -1.5[\![-w_n, 0]\!]/\Delta z - 0.5[\![-w_s, 0]\!]/\Delta z \tag{A.1- 1h}$$

$$F_{NN} = 0.5[\![-w_n, 0]\!]/\Delta z \tag{A.1- 1i}$$

where the superscript $*$ indicates that the coefficient is modified from that of inner control volumes. This formulation implements the algorithm more conveniently. For a control volume near the left boundary, we only convection coefficients with superscript $*$ need to be modified.

A.2 Right Border Control Volumes

Similarly, for a typical control volume adjacent to the right boundary, the discretization of the convection term along the axial direction remains unchanged as long as the control volume is not at the corner. In the radial direction, the second-order upwind scheme is still valid for the west face as two neighbours exists for both directions, i.e.

on the west face,

$$-\frac{u_w\phi_w}{\Delta r} = -(1.5\phi_W^{n+1} - 0.5\phi_{WW}^{n+1})[\![u_w, 0]\!]/\Delta r + (1.5\phi_P^{n+1} - 0.5\phi_E^{n+1})[\![-u_w, 0]\!]/\Delta r$$

remains unchanged.

On the east face, central difference is deployed when the flux u_e comes from the right boundary, i.e. $u_e < 0$, and second-order upwind is used when the flux u_e comes from the inner domain:

$$\frac{u_e T_e}{\Delta r} = (1.5T_P - 0.5T_W^{n+1})[\![u_e, 0]\!]/\Delta r - 0.5(T_E + T_P)[\![-u_e, 0]\!]/\Delta r$$

The convection term coefficients for control volumes adjacent to the right boundary $\boldsymbol{F}^{\text{right}}$ is written as

$$F_{SS} = 0.5[\![w_s, 0]\!]/\Delta z \tag{A.2- 1a}$$

$$F_S = -1.5[\![w_s, 0]\!]/\Delta z - 0.5[\![w_n, 0]\!]/\Delta z \tag{A.2- 1b}$$

$$F_{WW} = 0.5[\![u_w, 0]\!]/\Delta r \tag{A.2- 1c}$$

$$F_W = -0.5[\![u_e, 0]\!]/dr - 1.5[\![u_w, 0]\!]/\Delta r \tag{A.2- 1d}$$

$$\begin{aligned} F_P^* = {} & 1.5[\![u_e, 0]\!]/\Delta r + 1.5[\![-u_w, 0]\!]/\Delta r + 1.5[\![w_s, 0]\!]/\Delta z \\ & + 1.5[\![-w_n, 0]\!]/\Delta z - 0.5[\![-u_e, 0]\!]/\Delta r \end{aligned} \tag{A.2- 1e}$$

$$F_E^* = -.5[\![-u_e, 0]\!]/\Delta r - 0.5[\![-u_w, 0]\!]/\Delta r \tag{A.2- 1f}$$

$$F_{EE}^* = 0 \tag{A.2- 1g}$$

$$F_N = -1.5[\![-w_n, 0]\!]/\Delta z - 0.5[\![-w_s, 0]\!]/\Delta z \tag{A.2- 1h}$$

$$F_{NN} = 0.5[\![-w_n, 0]\!]/\Delta z \tag{A.2- 1i}$$

where the superscript $*$ indicates the coefficient is modified from that of inner control volumes.

A.3 Bottom Control Volumes

For a typical control volume adjacent to the bottom boundary, shown in Figure A.3, discretization for convection term along radial direction remains unchanged as long as the control volume is not at a corner. The discretization at the north face of the control volume cell can still deploy second-order upwind scheme, since two neighbours exist in each direction, thus

$$\frac{w_n \phi_n}{\Delta z} = (1.5\phi_P - 0.5\phi_S)[\![w_n, 0]\!]/\Delta z - (1.5\phi_N - 0.5\phi_{NN})[\![-w_n, 0]\!]/\Delta z$$

For the discretization at the south face of the control volume, if the flux w_s comes from the inner domain, i.e. $w_s < 0$, second order upwind scheme is used, otherwise if the flux w_s comes from the bottom boundary, i.e. $w_s > 0$, central difference is used.

$$-\frac{w_s \phi_s}{\Delta z} = -(0.5\phi_S + 0.5\phi_P)[\![w_s, 0]\!]/\Delta z + (1.5\phi_P - 0.5\phi_N)[\![-w_s, 0]\!]/\Delta z$$

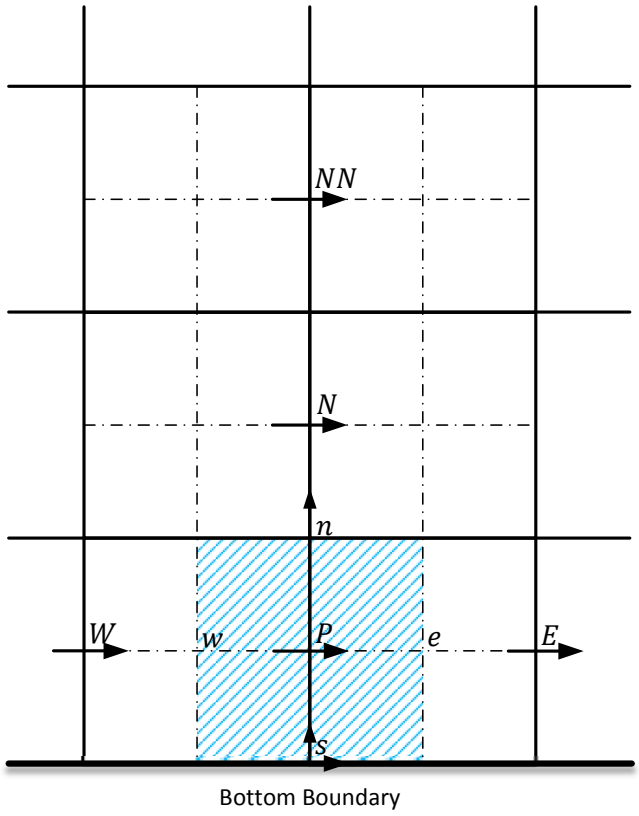

Figure A.3: Schematic of border (near boundary) control volume: a typical left border control volume

The convection term coefficients for a bottom border control volume is $\boldsymbol{F}^{\text{bottom}}$,

where the elements are

$$F^*_{SS} = 0 \tag{A.3- 1a}$$

$$F^*_S = -0.5[\![w_s, 0]\!]/\Delta z - 0.5[\![w_n, 0]\!]/\Delta z \tag{A.3- 1b}$$

$$F_{WW} = 0.5[\![u_w, 0]\!]/\Delta r \tag{A.3- 1c}$$

$$F_W = -0.5[\![u_e, 0]\!]/dr - 1.5[\![u_w, 0]\!]/\Delta r \tag{A.3- 1d}$$

$$F^*_P = 1.5[\![u_e, 0]\!]/\Delta r + 1.5[\![-u_w, 0]\!]/\Delta r + 1.5[\![w_n, 0]\!]/\Delta z + 1.5[\![-w_s, 0]\!]/\Delta z - 0.5[\![w_s, 0]\!]//\Delta z \tag{A.3- 1e}$$

$$F_E = -1.5[\![-u_e, 0]\!]/\Delta r - 0.5[\![-u_w, 0]\!]/\Delta r \tag{A.3- 1f}$$

$$F_{EE} = 0.5[\![-u_e, 0]\!]/\Delta r \tag{A.3- 1g}$$

$$F_N = -1.5[\![-w_n, 0]\!]/\Delta z - 0.5[\![-w_s, 0]\!]/\Delta z \tag{A.3- 1h}$$

$$F_{NN} = 0.5[\![-w_n, 0]\!]/\Delta z \tag{A.3- 1i}$$

A.4 Top Border Control Volumes

Similarly, for a typical control volume adjacent to the top boundary, discretization along radial direction remains unchanged as long as the control volume is not at a corner. For the axial direction, discretization at the south control volume face deploys second order upwind,

$$\frac{w_s\phi_s}{\Delta z} = -(1.5\phi_S - 0.5\phi_{SS})[\![w_s, 0]\!]/\Delta z + (1.5\phi_P - 0.5\phi_N)[\![-w_s, 0]\!]/\Delta z$$

On the north face,

$$\frac{w_n\phi_n}{\Delta z} = (1.5\phi_P - 0.5\phi_S)[\![w_n, 0]\!]/\Delta z - 0.5(\phi_N + \phi_P)[\![-w_n, 0]\!]/\Delta z$$

The convection term coefficients for a bottom border control volume is $\boldsymbol{F}^{\text{top}}$, where the elements are

$$F_{SS} = 0.5[\![w_s, 0]\!]/\Delta z \tag{A.4- 1a}$$

$$F_S = -1.5[\![w_s, 0]\!]/\Delta z - 0.5[\![w_n, 0]\!]/\Delta z \tag{A.4- 1b}$$

$$F_{WW} = 0.5[\![u_w, 0]\!]/\Delta r \tag{A.4- 1c}$$

$$F_W = -0.5[\![u_e, 0]\!]/dr - 1.5[\![u_w, 0]\!]/\Delta r \tag{A.4- 1d}$$

$$\begin{aligned} F_P^* &= 1.5[\![u_e, 0]\!]/\Delta r + 1.5[\![-u_w, 0]\!]/\Delta r \\ &+ 1.5[\![w_n, 0]\!]/\Delta z + 1.5[\![-w_s, 0]\!]/\Delta z - 0.5[\![-w_n, 0]\!]/\Delta z \end{aligned} \tag{A.4- 1e}$$

$$F_E = -1.5[\![-u_e, 0]\!]/\Delta r - 0.5[\![-u_w, 0]\!]/\Delta r \tag{A.4- 1f}$$

$$F_{EE} = 0.5[\![-u_e, 0]\!]/\Delta r \tag{A.4- 1g}$$

$$F_N^* = -0.5[\![-w_n, 0]\!]/\Delta z - 0.5[\![-w_s, 0]\!]/\Delta z \tag{A.4- 1h}$$

$$F_{NN}^* = 0 \tag{A.4- 1i}$$

A.5 Control Volume at Corners

For a control volume at a corner (red points shown in Figure A.1), since it is adjacent to two boundaries, the convection terms coefficients need modification in both axial and radial direction. For example, for the NW corner point, $F_W W, F_W, F_P, F_N, F_{NN}$ need to be modified. Details of the modification can be easily derived from our discussions above.

Appendix B

Annulus Fluids Properties Data

Table B.1: Air thermal properties at atmospheric pressure, data from The Engineering ToolBox [60]

Temperature (K)	Density (kg/m^3)	Specific Heat (kJ/kg.K)	Thermal Conductivity (W/m.K)	Dynamic Viscosity (Pa.s)	Expansion Coefficient (1E-3 1/K)	Prandtl's Number
273	1.293	1.005	0.0243	1.71969E-05	3.67	0.715
293	1.205	1.005	0.0257	1.82076E-05	3.43	0.713
313	1.127	1.005	0.0271	1.91252E-05	3.20	0.711
333	1.067	1.009	0.0285	2.01663E-05	3.00	0.709
353	1.000	1.009	0.0299	2.09423E-05	2.83	0.708
373	0.946	1.009	0.0314	2.18148E-05	2.68	0.703
393	0.898	1.013	0.0328	2.26565E-05	2.55	0.700
413	0.854	1.013	0.0343	2.35277E-05	2.43	0.695
433	0.815	1.017	0.0358	2.43278E-05	2.32	0.69
453	0.779	1.022	0.0372	2.51539E-05	2.21	0.69
473	0.746	1.026	0.0386	2.5834E-05	2.11	0.685
523	0.675	1.034	0.0421	2.77898E-05	1.91	0.68
573	0.616	1.047	0.0454	2.94756E-05	1.75	0.68
623	0.566	1.055	0.0485	3.11583E-05	1.61	0.68
673	0.524	1.068	0.0515	3.27657E-05	1.49	0.68

Table B.2: Nitrogen thermal properties at atmospheric pressure, data from an online thermodynamic properties calculator [53]

Temperature (K)	Density (kg/m^3)	Specific Heat (kJ/kg.K)	Thermal Conductivity (W/m.K)	Dynamic Viscosity (Pa.s)	Expansion Coefficient (1E-3 1/K)	Prandtl's Number
273	1.2503	1.0410	24.2307	16.6501	3.6608	0.7158
293	1.1660	1.0410	25.5986	17.5941	3.4243	0.7157
313	1.0920	1.0416	26.9306	18.5081	3.2050	0.7157
333	1.0262	1.0420	28.2305	19.3961	3.0114	0.7158
353	0.9672	1.0422	29.5025	20.2601	2.8382	0.7159
373	0.9146	1.0430	30.7505	21.1001	2.6741	0.7160
393	0.8686	1.0446	31.9745	21.9241	2.5478	0.7162
413	0.8267	1.0462	33.1804	22.7301	2.4246	0.7165
433	0.7894	1.0482	34.3684	23.5120	2.3148	0.7169
453	0.7553	1.0506	35.5444	24.2760	2.2144	0.7173
473	0.7212	1.0530	36.7204	25.0400	2.1069	0.7177
523	0.6582	1.0615	39.5953	26.8300	1.9295	0.7192
573	0.5953	1.0700	42.4703	28.6200	1.7392	0.7207
623	0.5511	1.0810	45.2953	30.2800	1.615	0.7227
673	0.5069	1.0920	48.1202	31.94	1.4800	0.7246

Table B.3: Water thermal properties at atmospheric pressure, data from [63] [61]

Temperature (K)	Density (kg/m^3)	Specific Heat (kJ/kg.K)	Thermal Conductivity (W/m.K)	Dynamic Viscosity (Pa.s)	Expansion Coefficient (1E-3 1/K)	Prandtl's Number
283.15	999.8	4.192	580	1.31	1.304	9.47
293.15	998.3	4.182	598.4	1	1.004	7.01
303.15	995.7	4.178	615.4	0.798	0.801	5.43
313.15	992.3	4.179	630.5	0.653	0.658	4.34
323.15	988	4.182	643.5	0.547	0.553	3.56
333.15	983	4.185	654.3	0.467	0.474	2.99
343.15	978	4.191	663.1	0.404	0.413	2.56
353.15	972	4.198	670	0.355	0.365	2.23
363.15	965	4.208	675.3	0.314	0.326	1.96

Table B.4: 11 lb/gal Calcium Chloride brine thermal properties at atmospheric pressure, data from [17]

Temperature (K)	Density (kg/m^3)	Specific Heat (kJ/kg.K)	Thermal Conductivity (W/m.K)	Dynamic Viscosity (Pa.s)	Expansion Coefficient (1E-3 1/K)
273.15	1318.086	2.6795	42.2305	13.51	0.46
283.15	1315.689	2.6962	42.9511	10.1	0.46
293.15	1312.094	2.7088	43.5276	8	0.46
303.15	1308.499	2.7214	44.1042	6.2	0.46
313.15	1304.905	2.7381	44.6807	5.1	0.46
323.15	1302.508	2.7507	45.2572	4.1	0.46
333.15	1298.913	2.7632	45.9779	3.5	0.46
343.15	1295.319	2.7800	46.5544	3.1	0.46
353.15	1291.724	2.7925	47.1309	2.8	0.46
363.15	1288.129	2.8051	47.7074	2.5	0.46
373.15	1285.732	2.8219	48.2840	2.3	0.46